Journal of Asian Earth Sciences 182 (2019) 103931

Contents lists available at ScienceDirect

Journal of Asian Earth Sciences

journal homepage: www.elsevier.com/locate/jseaes

Full length article

Origin of the Ediacaran Weng'an and Kaiyang phosphorite deposits in the Nanhua basin, SW China

Haiying Yang[a,b], Jiafei Xiao[a,*], Yong Xia[a], Zhuojun Xie[a], Qinping Tan[a], Jianbin Xu[a,b], Haiyan Guo[a,c], Shan He[a,b], Shengwei Wu[a,b]

[a] State Key Laboratory of Ore Deposit Geochemistry, Institute of Geochemistry, Chinese Academy of Sciences, Guiyang 550081, China
[b] University of Chinese Academy of Sciences, Beijing 101408, China
[c] School of Pharmacy, Chengdu University of Traditional Chinese Medicine, Chengdu 611137, China

ARTICLE INFO

Keywords:
Phosphorite
Apatite
Ediacaran
Doushantuo Formation
Central Guizhou

ABSTRACT

The Weng'an and Kaiyang phosphorite deposits are located in Central Guizhou, southwestern China, and formed within the Sinian (Ediacaran) Doushantuo Formation. A systematic investigation of the geology, mineralogy, and geochemistry of these phosphorites was conducted to constrain the redox environment, origin, and genetic mechanisms of Ediacaran phosphorite. In the lower ore layer (layer A), the phosphate minerals are mainly globular phosphate intraclasts, which are characterized by special sedimentary and reworking textures, including microgranular sedimentary, isopachous cement, shrinkage crack, and spongy texture. The phosphate minerals from the upper layer (layer B) have microbial phosphate components, namely embryo- and algae-like microfossils. These phosphatic microfossils have biological structures, and both consist of interior structure and isopachous wall. The P_2O_5 concentration of phosphorites in layer A reach 32.31%, somewhat higher than that in layer B (28.7%), whereas the P content in globular phosphate intraclasts (40.05%) resemble that of the microbial phosphate component (41.19%). Rocks from layer A have "left-inclining" post-Archean Australian shale (PAAS)–normalized rare earth element (REE) distributions, with higher Ce anomalies (Ce_{anom}) ranging from –0.12 to –0.01 (average –0.07). In contrast, rocks from layer B have "hat-shaped" PAAS–normalized REE distributions, with lower Ce_{anom} ranging from –0.32 to –0.23 (average –0.28). These geochemical characteristics suggest that hydrothermal fluids mixed with normal seawater might have contributed to metallogenesis, and the redox environment transitioned from anoxic to oxic from layer A to B. We conclude that the lower Doushantuo globular intraclasts formed by the mechanical reworking of previous phosphatic sediments, which were dominated by the strong mechanical power of seawater. The upper Doushantuo microbial phosphorite, on the other hand, formed by microbially mediated accretionary growth.

1. Introduction

The Doushantuo Formation, belonging to the Ediacaran that occurred around the Precambrian/Cambrian boundary (~541 Ma), was underlain by tillite of the Nantuo Formation and overlain by carbonates of the Dengying Formation. The Doushantuo carbonate–black shale–phosphorite sequence is widespread throughout southwestern China (Jiang et al., 2011), and represents the most important known phosphogenic event in geological history (Dong Ye, 2001). The marine sedimentary phosphorite in China mainly formed during the Ediacaran–Early Cambrian, accounting for more than 80% of the phosphorite resources in China (Dong Ye, 2001) and containing abundant middle–large phosphorite deposits. Four phosphorus-rich areas formed during the Ediacaran in southwestern China, including Central Guizhou (Fig. 1a), West Hunan (Fig. 1b), East Shanfeng (Fig. 1c), and West Hubei (Fig. 1d). In Central Guizhou, the phosphorite deposits are mainly located in Weng'an and Kaiyang.

The phosphate granules, previously regarded as collophane (Ye et al., 1986), are widely distributed in Southwest China within the Doushantuo Formation. Previous studies have suggested that the phosphate granules were related to the presence of microfossils, and the putative microfossils have since been reinterpreted as algae (Xue et al., 1995; Xiao et al., 1998; Mi et al., 2010; Igisu et al., 2014), animal embryos (Xiao et al., 1998; Yin et al., 2007a, 2007b; Igisu et al., 2014), acritarchs (Zhou et al., 2007; Muscente et al., 2015) and non-metazoan holozoans (Therese et al., 2012). She et al. (2013) studied the lower

* Corresponding author.
E-mail address: xiaojiafei@vip.gyig.ac.cn (J. Xiao).

https://doi.org/10.1016/j.jseaes.2019.103931
Received 10 August 2018; Received in revised form 1 July 2019; Accepted 21 July 2019
Available online 29 July 2019
1367-9120/

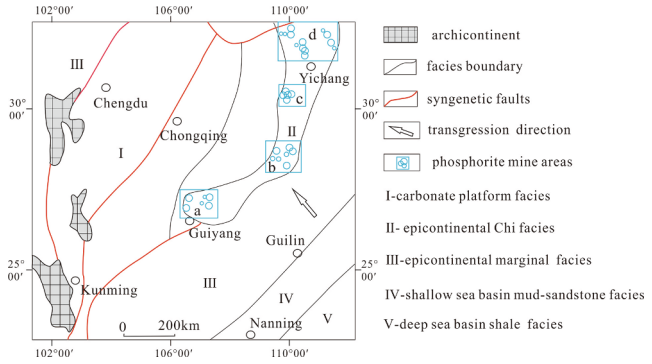

Fig. 1. Ediacaran lithofacies map of southwestern China and distributions of phosphorites (modified from Dong Ye (1996)).

layer of the phosphorites in the city of Yichang (Fig. 1d) using micro-analytical techniques and suggested that the apatite formed via biogenic accretion and precipitation. Muscente et al. (2015) compared the fossils preserved in phosphorites and silicolites in stratigraphic succession, paleogeographic distribution, preservation, and biodiversity, and suggested that the fossils preserved within the phosphorites experienced phosphatization from pore water influx.

However, several abiogenic phosphate granules have also been reported from the Doushantuo phosphorite deposits (Ye, 1989; Föllmi, 1996; Pufahl and Grimm, 2003; Chen et al., 2015). Observations made with transmitted light microscopy revealed that the phosphate granules of the lower layer were oval, with bright fibroid cements (Ye, 1989; Chen et al., 2015), and the cement was determined to be apatitic (She et al., 2013). At present, several models have been proposed to explain the formation of the phosphorites, including reworking of previous phosphate deposits (Follmi, 1996; Ilyin, 1998; Vernhet et al., 2007; She et al., 2013), in situ diagenetic mineralization driven by changes in pore water redox potential (Frohlich et al., 1983; Pufahl and Grimm, 2003; Muscente et al., 2015), and abiogenic accretion (Zhao, 1989). These views provide insight into the genetic mechanisms of Doushantuo phosphorite formation, but the genetic relationship between the biogenic and abiogenic phosphorites remains unclear. In part, this problem is likely due to the paucity of data on phosphorite mineralogy, and few studies have determined the specific micro-textures of the phosphate granules.

Previous geochemical studies of the Doushantuo phosphorite deposits in South China have suggested that they formed under anoxic conditions. Nathan and Nielsen (1980) and Benmore (1983) suggested that SO_4^{2-} isomorphically substituted PO_4^{3-} in carbonate–fluorapatite. Sulfur in marine sediments mainly originated from the reduction of sulfate in seawater. During sulfate reduction, the sulfur isotopic composition of sulfide and phosphorite depends on isotope fractionation (Strauss, 1999). The ^{32}S—O bonds are broken more easily than ^{34}S—O bonds are, and ^{32}S preferentially entered into S—S bonds (Harrison and Thode, 1958). Thus, under restricted sulfur concentrations, along with the process of sulfate reduction, more ^{34}S combined as S—S bonds along with the decreased ^{32}S, resulting to high $\delta^{34}S$ in S^{2-} and higher $\delta^{34}S$ in SO_4^{2-} (Strauss, 1999). Research has shown that $\delta^{34}S$ in apatite in the Doushantuo Formation ranged from +34.2 to +42.4‰ (Chu et al., 1995; Shi, 2005), which was higher than the $\delta^{34}S$ of contemporary seawater (+30‰) (Chu et al., 1995). Moreover, the $\delta^{34}S$ of the pyrite within the formation ranged from +15.4 to +19.8‰ (Shi, 2005). The $\delta^{34}S$ in both pyrite and apatite indicated that the phosphorites formed under anoxic sedimentary environments. Additional evidence includes organic matter in Weng'an phosphorites (Yin et al., 1999), the Ce anomaly (Ce_{anom} = 0.097–0.045), and the δU values (1.68–1.96) of Kaiyang phosphorite deposits (Deng et al., 2015). Nevertheless, a different viewpoint suggesting that the redox conditions transitioned from anoxic to oxic (Chen et al., 2003; Xie et al., 2003; Wu et al., 2006) has also been put forth. Wu et al. (2006) found that the concentrations of redox sensitive elements (RSEs), including Mo, U, and V, in the layer A of Weng'an phosphorite were higher than those in the layer B, and concluded that the redox conditions transitioned from anoxic to oxic. This finding is consistent with the fact that analyses of the Ce_{anom} revealed a change from –0.065–(–0.077) to –0.26–(–0.291) (Chen et al., 2003; Xie et al., 2003).

At present, there is no consensus on the origin of the metallogenic materials in the Doushantuo phosphorite deposits in southwestern China. There are four popular viewpoints: hydrothermal fluids (Yang et al., 1997; Guo et al., 2003; Shi, 2005; Yin et al., 2007a, 2007b), weathering of terrigenous rocks (Wang and Zhu, 1984; Wu et al., 1984; Yin et al., 2007a, 2007b), P-rich upwelling (Liu and Cao, 1987; Jiang et al., 2007), and Nantuo tillite (Wu et al., 1984; Yin et al., 2007a, 2007b). The evidence provided for hydrothermal fluids includes the following: (1) The enrichment of phosphorite in Weng'an with respect to SiO_2, Pb, Zn, Hg, As, and Ba, (Yang et al., 1997; Guo et al., 2003), which is consistent with the characteristics of hydrothermal sediments. (2) The tubular and alveolate eruption throats discovered in the Weng'an phosphorite mining area (Guo et al., 2003) and volcanic tuff in western Hunan (Yang et al., 1997), which provide direct evidence of hydrothermal activities during the deposition of the Doushantuo Formation. (3) The P_2O_5 content of the volcanic tuffs in the Banxi Group was 0.27%–0.65% in Weng'an, 1.5–3.6 times higher than that of the normal sediments (0.18%) (Yin et al., 2007a, 2007b). (4) The light rare earth element (LREE) / heavy rare earth element (HREE) ratio of Weng'an phosphorites ranged from 1.03 to 1.43, similar to those valves for the tuff (1.03) in the adjacent region in western Hunan (Guo et al., 2003). (5) The $^{87}Sr/^{86}Sr$ values of Doushantuo phosphorites were ~0.71 (Shi, 2005). These data suggest that volcanos erupted on the seafloor and brought fluids from the deep crust or mantle into the metallogenic region. The P_2O_5 contents of the West Sichuan and Central Yunnan old land surfaces were 1.4 times higher than that of the crust (Yin et al., 2007a, 2007b), indicating the weathering of terrigenous rocks as possible sources, which were then transported into the Yangtze area (Wang and Zhu, 1984; Wu et al., 1984). Additionally, Liu (1987) studied storm activities in early Cambrian oceans, and suggested that P-rich upwelling provided the main source of the phosphorites with the upwelling bringing ^{12}C-rich deeper seawater into shallow areas, resulting in the observed negative $\delta^{13}C_{carb}$ (−1.76‰) in Doushantuo carbonates, consistent with the results of Jiang et al. (2007) and Mi et al. (2010). Nantuo tillite is regarded as a potential source as the P_2O_5 of the tillite (0.09–0.21%) (Yin et al., 2007a, 2007b) is much higher than that of modern seawater (0.071×10^{-6}) (Wu et al., 1984).

Previous studies have conflicted in their assessment of the redox conditions, sources of metallogenic materials, and formation mechanisms of the phosphorite deposits in southwestern China. However, there are few reports on the micro-textures of the phosphorites in Central Guizhou. In this study, the Weng'an and Kaiyang phosphorite deposits in Guizhou were used as case studies, and both the apatite micro-textures and geochemical characteristics of the phosphorites were ascertained based on scanning electron microscopy (SEM), electron microprobe analysis (EMPA), and elemental geochemistry. The aim of this study is to reveal the redox conditions, the origin of the metallogenic materials, and the formation processes of the phosphorite deposits of the Ediacaran in Central Guizhou. The phosphorites from the upper and lower layers were subsequently compared by mineral features and geochemical characteristics to reveal the metallogenic mechanisms.

2. Geological setting

Central Guizhou is located in the interior of South China and in the west of Jiangnan Orogenic Belt (Fig. 2a). South China underwent multiple tectonic activities after Jinningian tectonics (900–820 Ma), during which time the ancient South China Plate formed due to the amalgamation of the Yangtze and the Cathaysia Blocks. Jinningian

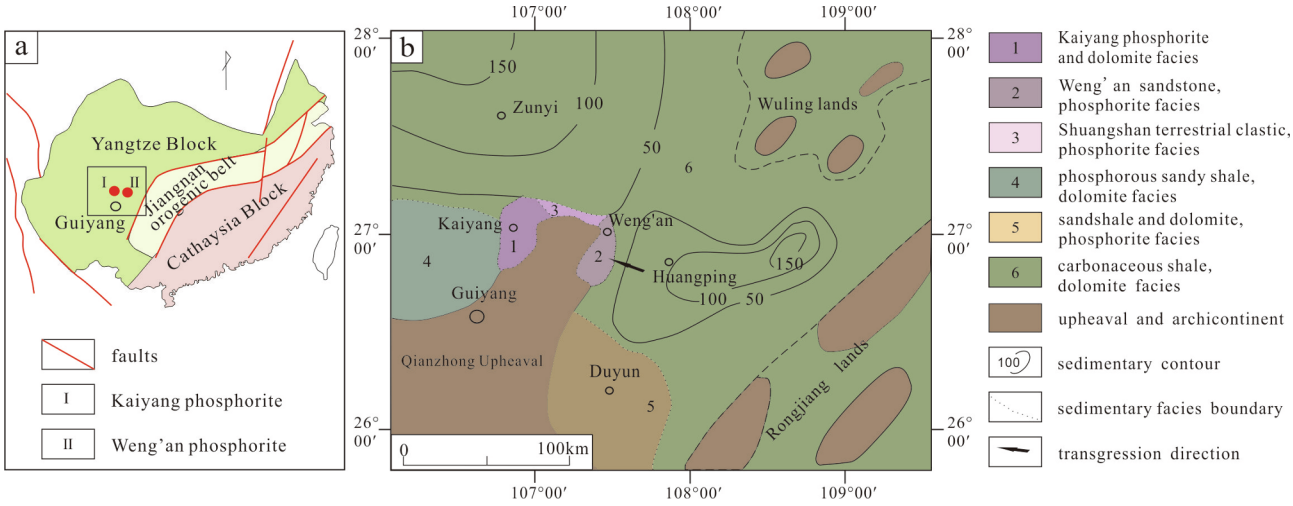

Fig. 2. a: Geological map of South China; b: Lithofacies paleogeographic map of Central Guizhou during the deposition of the Ediacaran Doushantuo Formation (modified from Ye et al. (1986)).

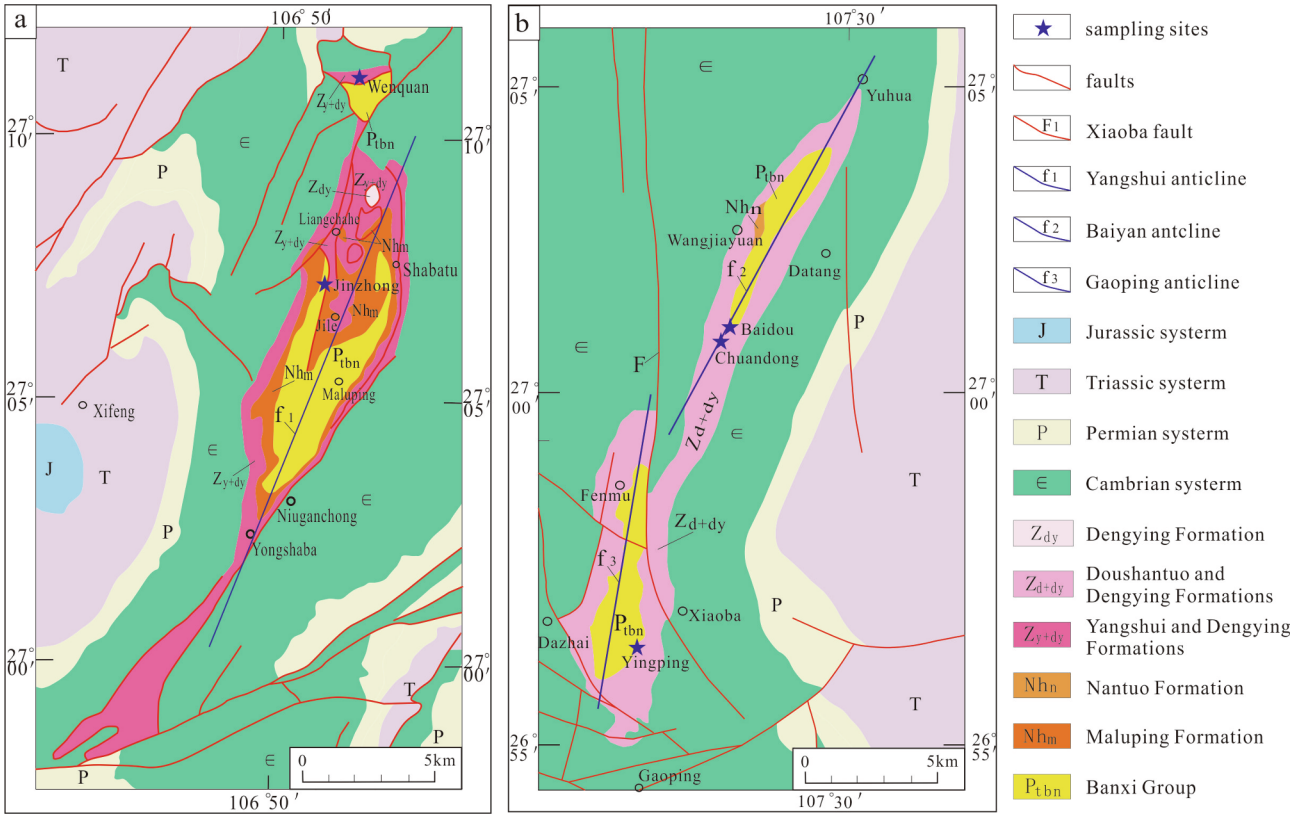

Fig. 3. a: Geological map of the Kaiyang phosphorus mining area. b: Geological map of the Weng'an phosphorus mining area.

tectonics caused the Jiangnan Orogenic Belt (Shu, 2012; Zhang et al., 2013). Thereafter, the ancient South China Plate rapidly underwent rifting and glaciation (Zhou and Wang, 2009; Shu, 2012). Along with the fragmentation of the supercontinent of Rodinia in the early Neoproterozoic, the Yangtze Block and Cathaysia Block began to break up, leading to Cryogenian rift systems (Wang and Li, 2003; Wang et al., 2006). Under these conditions, a series of graben–horst sub-basins progressively developed along the southeastern margin of the Yangtze Block (Jiang et al., 2003; Wang and Li, 2003; Zhang et al., 2013). The graben–horst sub-basins developed into small ocean basins (Liu et al., 1993), and the Jiangnan Orogenic Belt persisted as a series of submarine highlands during the Ediacaran Period (Dong Ye, 1996), with the seawater deepening from the northwest toward the southeast (Xue et al., 1995; Dong Ye, 1996). The western Hubei–Central Guizhou geotectogene was located within graben–horst sub-basins along the northwest side of the Jiangnan Orogenic Belt (Dong Ye, 1996, 2001), and was distributed across four P-rich areas distributing four P-rich areas (Fig. 1). The Qianzhong Uplift (Fig. 2b), which occurred within the interior of the western Hubei–Central Guizhou geotectogene, initially arose as a submarine rift zone during the Cryogenian, and was uplifted above sea level during the Ediacaran (He et al., 2005). Weng'an and Kaiyang phosphorite deposits are located along the northern margin of the Qianzhong Uplift of the Yangtze Block (Fig. 2b), belonging to a shallow marine platform environment (Ye et al., 1986;

Zhou, 1998) with moderate seawater depths.

The paleogeography of the Doushantuo controlled the formation and distribution of Weng'an and Kaiyang phosphorites. After the Marinoan glaciation, transgressions took place in Central Guizhou. Under the condition of transgressions, the Doushantuo phosphogenic event experienced three stages (Wang et al., 2016; Zhang et al., 2016). In the earlier depositional stage of the Doushantuo Formation, seawater coverage expanded due to frequent transgressions, and Weng'an and Kaiyang became tidal flats, with phosphate sedimentation. In the middle depositional stage of the Doushantuo Formation, Kaiyang was aerially exposed as regressions occurred, while Weng'an became a supratidal flat, forming dolomite sediments. In the later depositional stage of the Doushantuo Formation, transgressions occurred again, and microorganism thrived in Weng'an, forming a biogenic phosphorite layer. Similarly, Kaiyang became a tidal flat, and also developed phosphate sediments (Wang et al., 2016).

3. Phosphorite deposits

Kaiyang phosphorites are located at the wings and core of the Yangshui Anticline (Fig. 3a, f1). The distribution of phosphorite ore blocks is controlled by the Yangshui Anticline and several regional NE-trending faults. The Wenquan, Liangchahe, Shabatu, Jile, Maluping, Niuganchong, and Yongshaba ore blocks are also distributed along the anticline (Fig. 3a). The Weng'an phosphorite deposit is controlled by the Baiyan–Gaoping Anticline (Fig. 3b), which is crosscut by the NE-trending Xiaoba Fault (Fig. 3b, F1) and divided into the Baiyan Anticline (Fig. 3b, f2) and Gaoping Anticline (Fig. 3b, f3). The Yuhua, Wangjiayuan, Datang, Chuandong, Fenmu, Xiaoba, Yingping, and Dazhai ore blocks are distributed within the core of the Baiyan–Gaoping Anticline (Fig. 3b).

Doushantuo strata lie disconformably above the tillite of the Nantuo Formation and conformably beneath the carbonates of the Dengying Formation. The Doushantuo Formation is divided into four lithostratigraphic members, and the thicknesses of ore-bearing rock series range from 28.3 to 36.1 m (Fig. 4). The lithology and sedimentary facies from the Member I to Member IV change as follows. In Member I, the rock is a cap dolostone, mainly composed of dolomite, siliceous shale with cross-bedding, horizontal bedding, and microscale-wavy bedding, indicating that the rocks formed in a tidal flat environment during an early transgression. Member II (the layer A) has a thickness of 0–17.8 m. The rock series are mainly composed of grainy phosphorite with parallel bedding (Fig. 5a) and horizontal bedding (Fig. 5b), which represents a shallow subtidal environment with increased hydrodynamic forces. Member III (serving as the interlayer) is composed of dolostone, siliceous dolostone, and chert, indicating a supratidal flat environment resulting from a decrease in sea level (i.e., a regression). Member IV (the layer B) has a thickness of ~11.5 m. Cross-bedding (Fig. 5c), cataclastic structures, (Fig. 5d and e), and a spherulitic texture (Fig. 5f and g) are prevalent in the middle of layer B, indicating an intertidal flat with strong mechanical power as the depositional environment. In the uppermost part of layer B, the rock consists of phosphoric dolostone and dolostone, indicating a supratidal flat along with regression. The mineralogical features reflect the mechanical power of seawater, indicating that the phosphorites in the Doushantuo Formation were formed under tidal flat conditions resulting from cyclic marine transgressions and regressions.

Phosphorites mainly occur in Members II and IV, and their lithology is described in Fig. 4. The phosphorite displays compact banded, massive, cataclastic, and spherulitic structures. The banded structure (Fig. 5h and i) is the most prominent structure and consists of alternating 1–5 mm bands. The dark bands are composed of collophane and the light bands are composed of dolomite and lithified detritus. Ores with thin bands (less than 1 mm) are called striped ores (Fig. 5j). The massive structure (Fig. 5k and l) consists of fine-grained sand-sized phosphorite. The banded and massive phosphorites are generally high-grade ores and occur throughout the entire Doushantuo phosphatic strata. The cataclastic structure (Fig. 5d and e) consists of 2–5 mm clasts and dolomite veins. The spherulitic structure (Fig. 5f and g) is composed of 0.5–2 mm macroscopic spherulites. Both spherulitic and cataclastic ores are found in the upper layer of the Baidou ore block.

Based on mineral constituents and structures, the Doushantuo phosphorites were divided into four types, namely grainy phosphorite, biological phosphorite, cataclastic phosphorite, and individual phosphatic detritus. The grainy phosphorite (i.e., the main rock type) is distributed throughout the Doushantuo phosphorite-bearing strata, whereas the biological phosphorite, cataclastic phosphorite, and phosphatic detritus are distributed only within layer B. The wall rocks comprise P-rich silicates, quartzites, phosphatic dolostones, and siliceous dolostones (Table 1).

4. Sampling and analytical methods

4.1. Sampling sites

Samples were collected from the following ore blocks (Fig. 3; marked with blue stars): the Baidou ore block (N = 12; samples 1–4 were from ore layer A and samples 6–12 were from ore layer B), the Chuandong ore block (N = 4; all samples were from ore layer A), the Yingping ore block (N = 7; sample 1 was from ore layer A and samples 4–7 were from ore layer B), the Jinzhong ore block (N = 5; all samples were from ore layer B), and the Wenquan ore block (N = 6; all samples were from ore layer A). Four wall rocks were also sampled, including samples BD–5 (Baidou), JZ–6 (Jinzhong), and YP–2 and YP–3 (Yingping). The sampling sites are shown in Fig. 6, with Jinzhong and Baidou given as examples because they are well-exposed, fresh, and sequential.

4.2. Analytical methods

All samples were sieved using 200 mm-mesh for analyzing major and trace elements, and portions of the samples from the Baidou and Jinzhong ore blocks were made into polished thin sections for observing mineral textures. Major elements were analyzed at ALS Minerals (Guangzhou) Co., Ltd, and trace element analyses, EMPA, and SEM were conducted at the State Key Laboratory of Ore Deposit Geochemistry of the Institute of Geochemistry, Chinese Academy of Sciences.

The major components of phosphorite, including SiO_2, Al_2O_3, TiO_2, TFe, MnO, CaO, MgO, K_2O, and P_2O_5, as well as the loss on ignition (LOI), were analyzed through X-ray fluorescence (XRF; ME-XRF24). The major components of the wall rocks were also analyzed through XRF (ME-XRF26). The phosphorite samples were digested by a $LiNO_3$ solution (the wall rocks were digested by $Li_2B_4O_7$) and then melted at 1000 °C. The other samples were burned at 1000 °C to acquire the LOI. The sum of XRF analyses and LOI was considered as the "total." The detection limit for all major oxides is 0.01 wt% and the error are less than 3%.

Trace elements were analyzed by Quadrupole Inductively Coupled Plasma Mass Spectrometer (Q-ICP-MS), model ELAN-DRC-e ICP-MS, with a relative standard deviation of generally better than 10%. Portions (50 mg) of the samples were completely digested using a mixed HF and HNO_3 solution, and the internal standard was a 40 ng/ml Rh solution; the methodology followed that of Qi et al. (2000). The detection limits are as follows: Tb, Ho, Lu, Cs, and Tm (0.01 ppm); Er, Eu, Sm, Pr, and Yb (0.03 ppm); Ba, Ce, Co, Th, Gd, Dy, and U (0.05 ppm); Rb, Cu, Ni, Nb, and Hf (0.2 ppm); Ta, Nd, Ga, and Sr (0.1 ppm); Y, Tl, Pb, and La (0.5 ppm); Zr and Mo f(2 ppm); W and Sn (1 ppm); V (5 ppm); Cr (10 ppm).

The micro-textures of minerals were observed using a JSM-7800F field emission SEM. The beam emitted by the electric gun was turned into a high-energy electric beam by a 10–30 KV acceleration voltage,

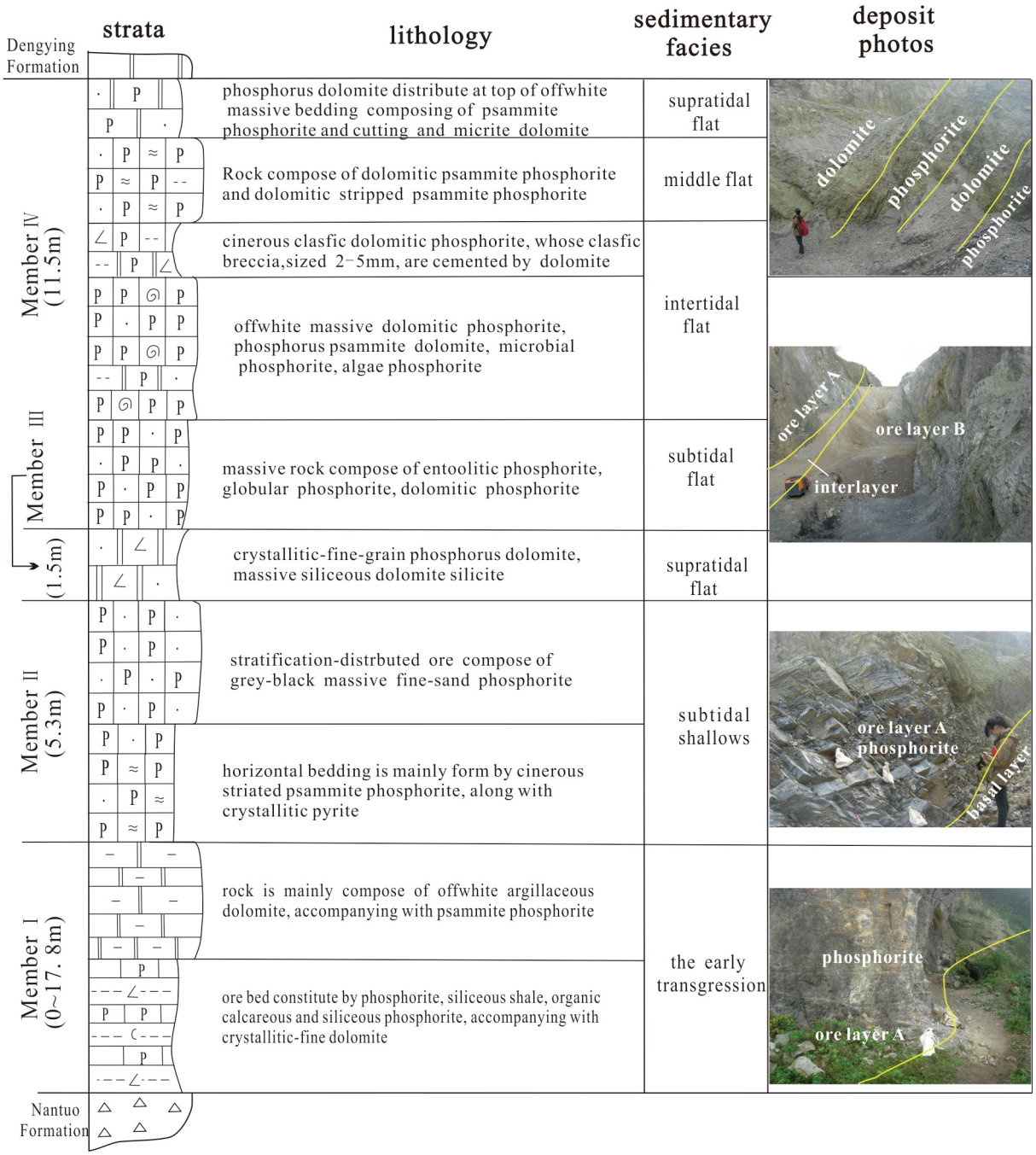

Fig. 4. Stratigraphy and sedimentary facies profile of the Ediacaran Baidou ore block of the Doushantuo Formation in Weng'an.

and then focused as a 1-μm microbeam to bombard the surface of the mineral. The secondary and backscattered electrons were detected and analyzed by the SEM. The backscattered electron image (BSE) was collected with a 10 Kv, 4.5 mA beam current, and the secondary electron image (SEI) was collected with a 20 Kv, 4.5 mA beam current.

The in situ major elements of phosphate minerals were analyzed by the EPMA-1600 produced by Shimadzu corporation of Japan. The high-pressure beam emitted by the electric gun bombarded the surface of the mineral, exciting characteristic X-rays, and the X-ray signals were collected at an accelerating voltage of 10 kV and a 4.5 mA beam current. The measured elements were F, P, Ca, Mg, Si, Mn, Al, S, La, Ce, Pr, Nd, and Th. We used an apatite standard for F, P, Ca, and Mg contents and the detection limit was 0.1 wt%.

5. Results

5.1. Collophane micro-textures

Phosphate minerals, appearing as microcrystalline to fine-grained aggregates, were typically designated as collophane (Ye et al., 1986) because they appear to be homogeneous under a polarized light microscope. The ore mineral of the phosphorites is collophane, and the gangue minerals are mainly dolomite, with trace amounts of pyrite, chalcopyrite, quartz, and clay minerals. The phosphate particles from the sedimentary phosphorites were divided into globular globular phosphate intraclasts and microbial phosphate components according to the observed micro-textures.

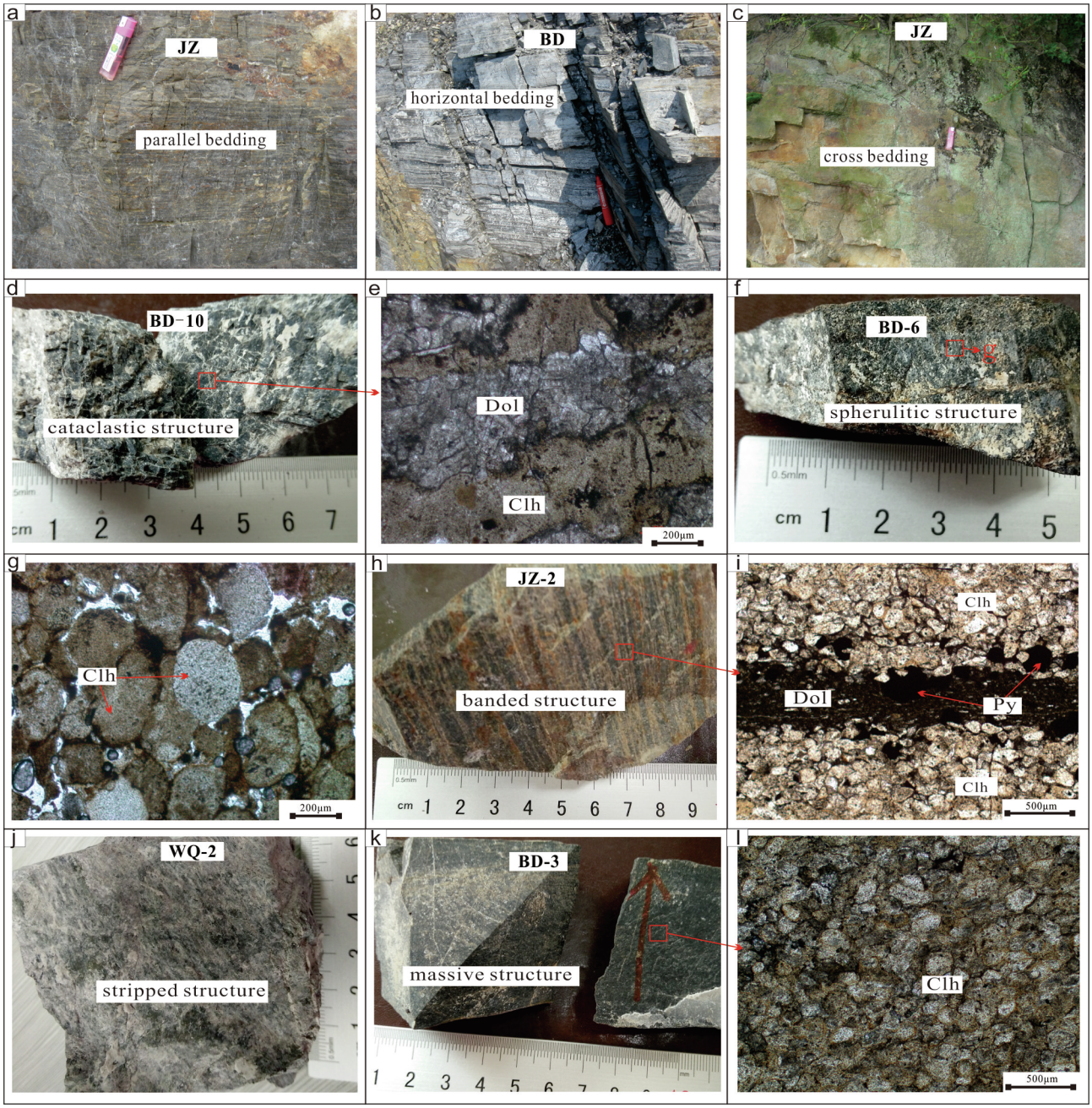

Fig. 5. Structures of the Doushantuo phosphorite in Central Guizhou (Yangtze Block) and photomicrographs of the phosphorites (e, g, i, and l are under transmitted light, plane polarized). (a) parallel bedding in ore layer A; (b) horizontal bedding in layer A; (c) cross-bedding in ore layer A; (d and e) cataclastic phosphorite; (f and g) spherulitic texture; (h and i) banded structure; (j) striped structure; (k and l) massive structure. In all images, Clh represents collophane, Dol represents dolomite, Py represents pyrite, BD represents the Baidou ore block, JZ represents the Jinghong ore block, and WQ represents the Wenquan ore block.

5.1.1. Globular phosphate intraclasts

The globular phosphate intraclasts are distributed throughout the Doushantuo phosphorite-bearing strata, but mainly in layer A. The phosphate granules, deemed as abiogenic, have approximately stable diameters of 50–550 μm and are in close contact with each other (Fig. 7a). Partial phosphate granules are inlaid in dolomite (Fig. 7b), exhibiting gray contrast whereas the dolomite showed dark-gray contrast in BSE images.

The primary sedimentary fabrics were observed in almost all the globular phosphate intraclasts, including microgranular sedimentary texture (Fig. 7c and d), shrinkage cracks (Fig. 7e and f), a spongy texture (Fig. 7g and h), and isopachous cements (Fig. 7e, f, and i). The microgranular sedimentary texture was observed in most globular phosphate intraclasts. In the microgranular sedimentary texture (Fig. 7d), dark particles were found to be attached to the mineral grains. The shrinkage cracks (Fig. 7f), with widths of 1–2 μm, are chiefly distributed in the inner globular phosphate and rarely distributed in the exterior cements. The spongy texture (Fig. 7g and h) is distributed mainly in the inner globular phosphate intraclasts. Most of the granules are surrounded by a bright isopachous cement and contained fibrous apatite crystals (Fig. 7i). The isopachous cement (Fig. 7e and f) is characterized by abundant, well-ordered, globular and prismatic microcrystalline apatite (1–2 μm wide and up to ~10 μm long), serving as the first-generation. The second-generation consist of dolomite occupying interstitial spaces among phosphate intraclasts (Fig. 7b). Additionally, pyrite is very common in the samples from layer A but rare

Table 1
Major element analyses of phosphorites from Central Guizhou, Doushantuo Formation, Ediacaran (wt.%).

Sampling Sites		Rock types	Al_2O_3	BaO	CaO	F	TFe_2O_3	K_2O	MgO	MnO_2	Na_2O	P_2O_5	SiO_2	SO_3	TiO_2	LOI
YP-1		Grainy phosphorite	0.73	0.06	49.42	3.5	0.89	0.27	0.29	0.13	0.35	35.18	6.49	0.48	0.05	2.77
YP-4	Ore layer B	Grainy phosphorite	0.12	0.08	53.79	3.7	0.06	0.05	0.12	0.01	0.41	39.40	0.60	0.50	0.02	2.22
YP-5		Grainy phosphorite	0.18	0.08	53.87	3.6	0.05	0.06	0.12	0.01	0.41	39.38	0.54	0.51	0.02	2.26
YP-6		Grainy phosphorite	0.47	0.09	52.64	3.6	0.54	0.14	0.15	0.02	0.37	38.68	1.75	0.45	0.11	2.13
YP-7		Grainy phosphorite	0.46	0.07	52.91	3.6	0.44	0.14	0.12	0.01	0.32	38.59	1.61	0.43	0.09	2.16
BD-1	Ore layer A	Grainy phosphorite	2.00	0.08	44.77	3.1	0.84	0.78	1.64	0.08	0.41	30.68	10.60	1.39	0.11	5.56
BD-2		Grainy phosphorite	2.01	0.20	45.83	3.2	0.45	0.68	0.81	0.05	0.43	32.34	9.98	0.99	0.10	3.92
BD-3		Grainy phosphorite	1.31	0.11	48.09	3.4	0.37	0.48	0.75	0.06	0.43	33.85	6.93	0.71	0.08	4.26
BD-4		Grainy phosphorite	1.54	0.46	47.61	3.1	0.23	0.54	0.87	0.07	0.44	33.46	7.30	0.68	0.09	4.21
BD-6	Ore layer B	Biological phosphorite	0.44	0.08	51.63	3.1	0.32	0.14	0.26	0.02	0.50	37.68	1.72	0.42	0.04	3.98
BD-7		Biological phosphorite	0.47	0.07	53.16	3.2	0.16	0.17	0.24	0.01	0.53	38.77	1.18	0.51	0.05	2.64
BD-8		Biological phosphorite	0.08	0.02	38.9	–	0.13	0.03	13.90	0.04	0.10	13.95	1.13	0.16	< 0.01	30.67
BD-9		Biological phosphorite	0.06	0.02	41.8	–	0.08	0.03	11.30	0.03	0.14	18.95	0.70	0.21	< 0.01	25.72
BD-10		cataclastic phosphorite	0.09	0.04	43.12	2.0	0.10	0.04	9.17	0.05	0.33	21.94	0.50	0.29	0.01	22.41
BD-11		Biological phosphorite	0.19	0.02	36.81	1.1	0.16	0.08	14.75	0.04	0.11	11.35	0.80	0.17	0.01	34.05
BD-12		Biological phosphorite	0.40	0.02	37.12	1.6	0.16	0.14	9.73	0.02	0.09	17.00	11.35	0.15	0.02	22.29
JZ-1	layer A	Grainy phosphorite	1.08	0.04	49.84	3.8	0.76	0.22	0.13	0.09	0.29	36.93	3.92	0.41	0.08	2.36
JZ-2		Grainy phosphorite	1.16	0.04	49.56	3.7	1.56	0.29	0.19	0.11	0.30	36.03	3.89	0.44	0.10	2.63
JZ-3	Ore layer A	Grainy phosphorite	0.80	0.04	51.74	3.6	0.87	0.20	0.19	0.08	0.34	36.69	3.08	0.47	0.06	2.99
JZ-4		Grainy phosphorite	0.77	0.05	52.66	3.3	0.22	0.16	0.16	0.06	0.37	38.25	2.28	0.48	0.06	2.28
JZ-5		Grainy phosphorite	0.91	0.08	51.36	3.6	1.20	0.24	0.21	0.19	0.32	37.35	2.14	0.50	0.06	2.32
CD-1	Ore layer A	Phosphorus detritus	12.05	0.31	16.71	1.2	2.57	2.78	2.25	0.05	0.14	10.99	43.0	0.38	0.55	7.32
CD-2		Clastic phosphorite	7.04	0.05	29.01	1.8	2.39	1.93	2.35	0.10	0.23	19.54	28.3	2.49	0.36	7.55
CD-3		Clastic phosphorite	6.33	0.07	31.38	1.9	2.09	2.81	2.28	0.12	0.27	21.13	24.7	2.42	0.29	6.76
CD-4		Grainy phosphorite	2.16	0.05	45.16	3.0	1.18	0.83	0.83	0.07	0.40	32.18	10.25	1.49	0.12	3.85
WQ-1	Ore layer A	Grainy phosphorite	0.66	0.41	46.67	3.0	0.70	0.22	3.26	0.21	0.22	30.57	6.38	1.44	0.05	7.75
WQ-2		Grainy phosphorite	0.68	0.61	48.28	3.3	2.63	0.23	1.17	0.07	0.20	34.36	4.65	3.21	0.06	3.86
WQ-3		Grainy phosphorite	0.81	0.17	49.02	3.3	2.51	0.28	1.26	0.06	0.17	34.44	4.03	3.05	0.07	4.03
WQ-4		Grainy phosphorite	0.49	0.43	50.73	3.5	2.17	0.17	0.96	0.04	0.05	36.95	2.29	2.81	0.04	2.83
WQ-5		grainy phosphorite	0.21	0.03	52.30	3.7	0.44	0.08	0.26	0.04	0.42	37.49	3.03	0.46	0.02	2.04
WQ-6		Grainy phosphorite	0.62	0.13	51.84	3.3	0.89	0.21	0.84	0.04	0.06	37.84	2.32	1.33	0.05	2.35
		Average value	1.46	0.13	45.58	2.98	0.87	0.46	2.68	0.07	0.29	30.59	7.47	0.93	0.09	7.65
		Average value of layer A	2.17	0.17	45.60	3.12	1.25	0.67	1.04	0.09	0.29	32.31	9.28	1.28	0.12	4.08
		Average value of layer B	0.27	0.05	46.89	2.83	0.20	0.09	5.44	0.02	0.30	28.70	1.99	0.35	0.04	13.68
YP-2	Wall rocks	Phosphorus silicate	0.42	0.04	30.69	1.6	0.67	0.14	5.23	0.13	0.16	16.98	31.6	0.27	0.03	12.49
YP-3		Quartzite	0.03	< 0.01	< 0.01	–	< 0.01	< 0.01	< 0.01	< 0.01	< 0.01	0.02	98.66	< 0.01	< 0.01	0.35
BD-5		Phosphorus dolomite	0.48	0.02	32.9	–	0.47	0.16	14.15	0.11	0.07	9.00	9.59	0.14	0.02	32.12
JZ-6		Siliceous dolomite	< 0.01	< 0.01	29.8	–	0.12	0.01	20.7	0.06	0.01	0.50	3.89	0.08	< 0.01	44.39

in the samples from layer B. Pyrite is 10–80 μm in diameter and inlaid in the dolomite and globular phosphate intraclasts (Fig. 7b). The microcrystalline apatite, 1–8 μm in diameter, formed through phosphatization during the diagenesis. The crystallites sustain their intact crystallographic forms, and the textures include granular (Fig. 7k), short six-sided columnar (Fig. 7l), radial (Fig. 7m), botryoidal (Fig. 7n), and thick sheets (Fig. 7o).

5.1.2. Microbial phosphate components

The microbial phosphate component, distributed in layer B, was considered as embryo- and algal-like microfossils through morphological comparison with previous studies. In the optical photomicrographs, embryo-like fossils appeare as globular and brownish to yellow-black under plane polarized light (Fig. 8a–c). In Weng'an phosphorite, the embryo-like fossils are pelletiod (Fig. 8a and b) and ~400 μm in diameter. The embryo-like fossils are comprised an inner core and isopachous cement, with a thickness of 10 μm. In the inner core, two-cell texture (Fig. 8a), four-cell texture (Fig. 8b), eight-cell texture and closely packed multi-cell texture (Fig. 8c) were observed. Under SEM, embryo-like microfossils were found to consist of an inner core and isopachous apatite wall (Fig. 8d and e). Some researchers have explained these fossils as diapause egg cysts or hulls (Xiao et al., 1998; Yin et al., 2007a, 2007b), similar to the growing textures produced by a phylogenetically disparate array of aquatic invertebrates (Van Waveren and Marcus, 1993; Zhou et al., 2007). The textures of the embryo-like microfossils in Doushantuo phosphorite are consistent with these growing textures.

The algal-like microfossils in the Doushantuo Formation range from simple to aggregated entities. The simple entities, referred to as "incipient tissues" of algae, appear as concentric ring-like (Fig. 8f), pistil-like (Fig. 8g), irregularly concentric (Fig. 8h), cell-stacked (Fig. 8i), and petaloid (Fig. 8j) forms. The concentric ring-like form (Fig. 8f), which is approximately 20 μm in diameter, generally consists of two concentric rings (gray contrast) and inner algae (dark contrast). Each ring is composed of apatite bunch cemented by 0.2 × 5 μm alternating columnar, microcrystalline apatite. The internal and external relationships of the rings may represent the sequential growth order of apatite rings. In the pistil-like form (Fig. 8g), algae with a 3–5 μm diameter (dark contrast, red arrows) are stacked together, and the light-colored apatite grow around the algae. The irregularly concentric form (Fig. 8h), approximately 5–25 μm in diameter, consiste of alternately irregular annuli (gray contrast) and inner microorganism remains (dark

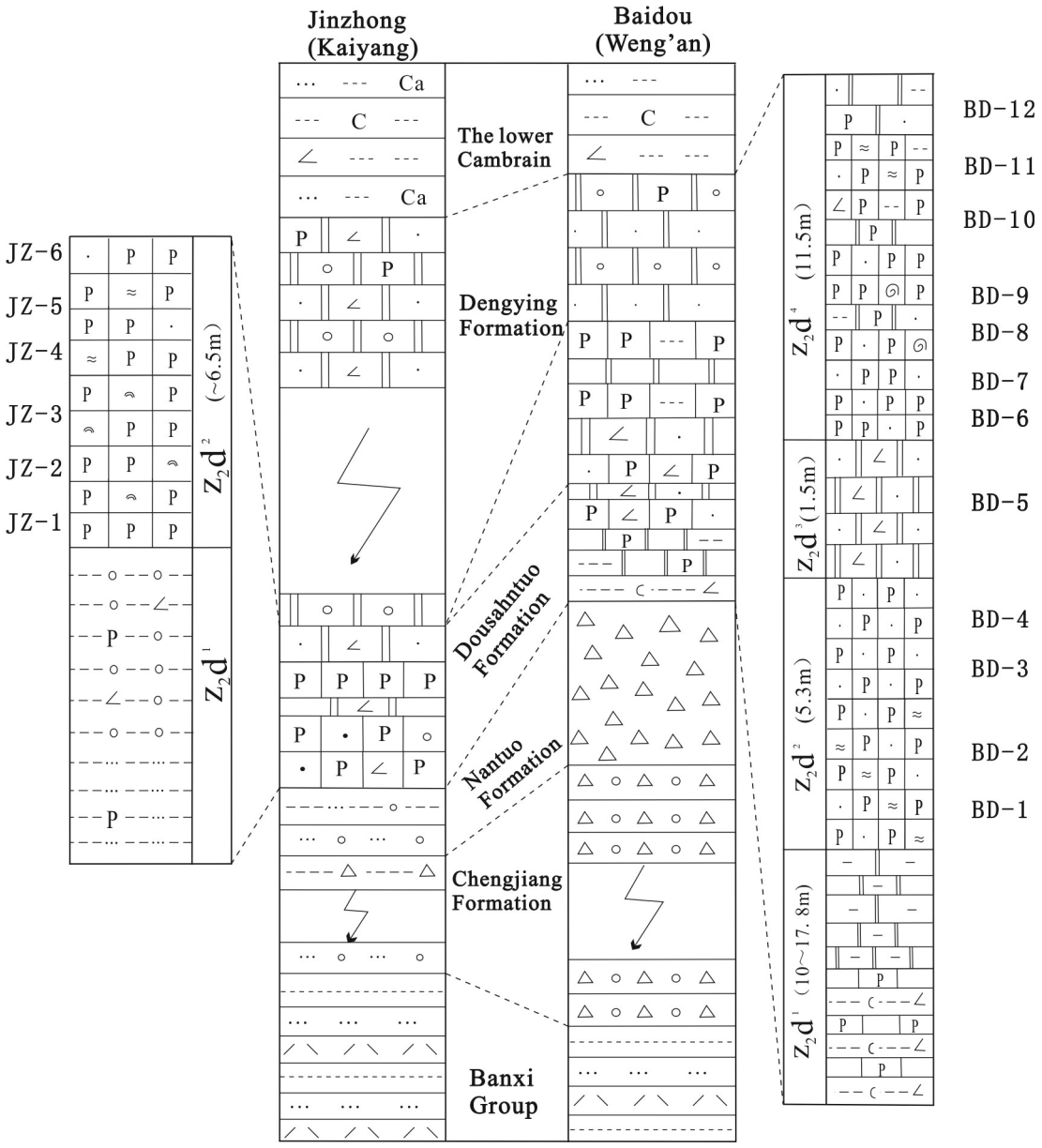

Fig. 6. Schematic diagram of sampling along the profiles of the Baidou and Jinzhong ore blocks.

contrast, red arrows). The cell-stacked form (Fig. 8i), comprise closely stacked cubes, 2–5 μm in diameter. These kinds of incipient tissues have been recognized as algal tissues (Xiao et al., 1998; Xiao and Knoll, 2000) recording the primary cell cleavage. The petaloid apatite (Fig. 8j), approximately 20 μm in diameter, consiste of an isopachous cement, a crossed septal and hollow texture, and the basal crossed septa of completely preserved microorganisms, causing the apatite to appear petal-like. Metallic minerals, such as chalcopyrite and ferric oxide, are inlaid in the apatite. The petaloid apatites were identified as simple colonial spheroids in tetrads (She et al., 2013, 2014). In the aggregated entities (Fig. 8k–o), 1–2 mm in diameter, many of the above textures are included in the interior and one light-colored, isopachous cement (5–10 μm wide) curved around and encompassed the algae clusters. The isopachous cement consiste of a light-colored apatite bunch, similar to the globular phosphate intraclasts. Some concentrically zoned granules are observed under SEM (Fig. 8p), which is consistent with granules from Yichang phosphorite (She et al., 2013). A small portion of algae were damaged and maintained only fragmentary granules (Fig. 8q). In the upper layer, the amorphous apatite with gray–white contrast is prevalent (Fig. 8r), mutually cemented with dolomite and serving as the second-generation cement.

5.2. *In situ major elements*

The major elements of phosphate minerals were analyzed via EMPA. The average (which represents the mean value throughout the paper) contents of F, P_2O_5, and CaO in phosphorite for globular intraclasts are F = 3.94%, P_2O_5 = 40.05%, and CaO = 53.36% and F = 3.70%, P_2O_5 = 41.19%, and CaO = 53.90% for microbial phosphate, showing slightly higher F and slightly lower P_2O_5 contents in globular phosphate intraclasts than in microbial phosphates (Table 2). Using EMPA, the Al_2O_3 and SiO_2 contents in the collophane are characterized by coordinated variation and showed negative correlations with P_2O_5 (Fig. 9). The F and P_2O_5 contents of globular phosphate intraclasts resemble the microbial phosphate component, indicating that the P content has no connection to the different genetic mechanisms and that the genetic mechanism may not be the reason for the change in P_2O_5 content from layer A to B. Linear principal component analyses (Fig. 10) of the irregular annuli suggest that

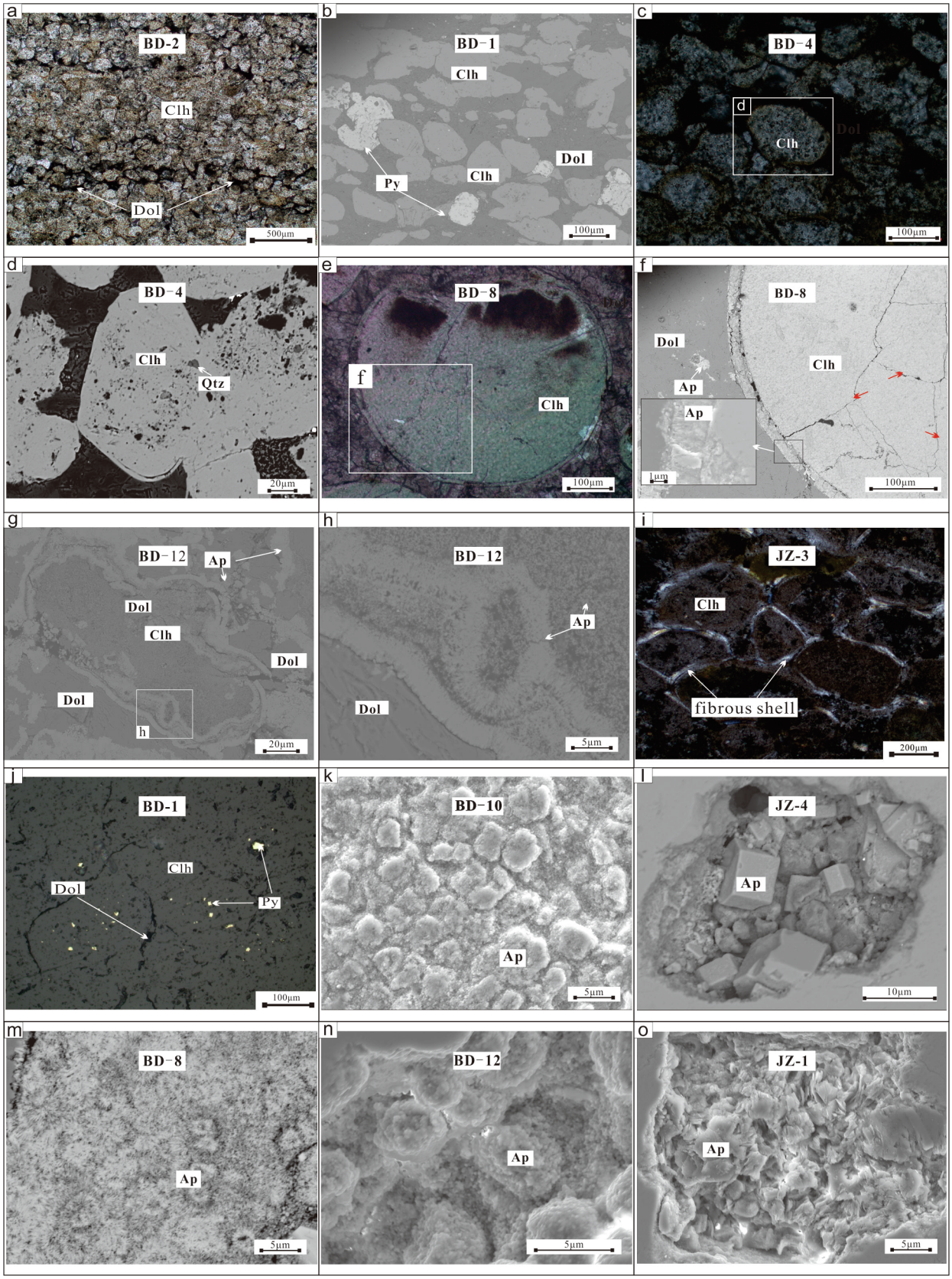

Fig. 7. Microstructure of globular phosphate intraclasts of the Doushantuo Formation phosphorites. (a, c, e, and i are under transmitted light, a is under cross-polarized light, c, e, and i are under plane polarized light; j is under emitted light; b, d, f, g, and h are backscattered electron images; k, l, m, n, and o are secondary electron images). (a) Ore grain; (b) automorphic crystals of globular phosphate intraclasts; (c and d) microgranular sedimentary structure texture; (e and f) isopachous cement and shrinkage cracks of globular phosphate intraclasts, squares show the locations of magnified views in (f); (g and h) spongy structure, (h) magnified image of (g); (i) bright fibrous cement around the globular phosphate intraclasts; (j) pyrite; (k) granular microcrystalline apatite; (l) short six-sided columnar microcrystalline apatite; (m) radial microcrystalline apatite; (n) botryoidal microcrystalline apatite; (o) thick sheet of microcrystalline apatite. BD represents the Baidou ore block, JZ represents the Jinzhong ore block, Ap represents apatite, Dol represents dolomite, Chl represents collophane, and Qtz represents quartz.

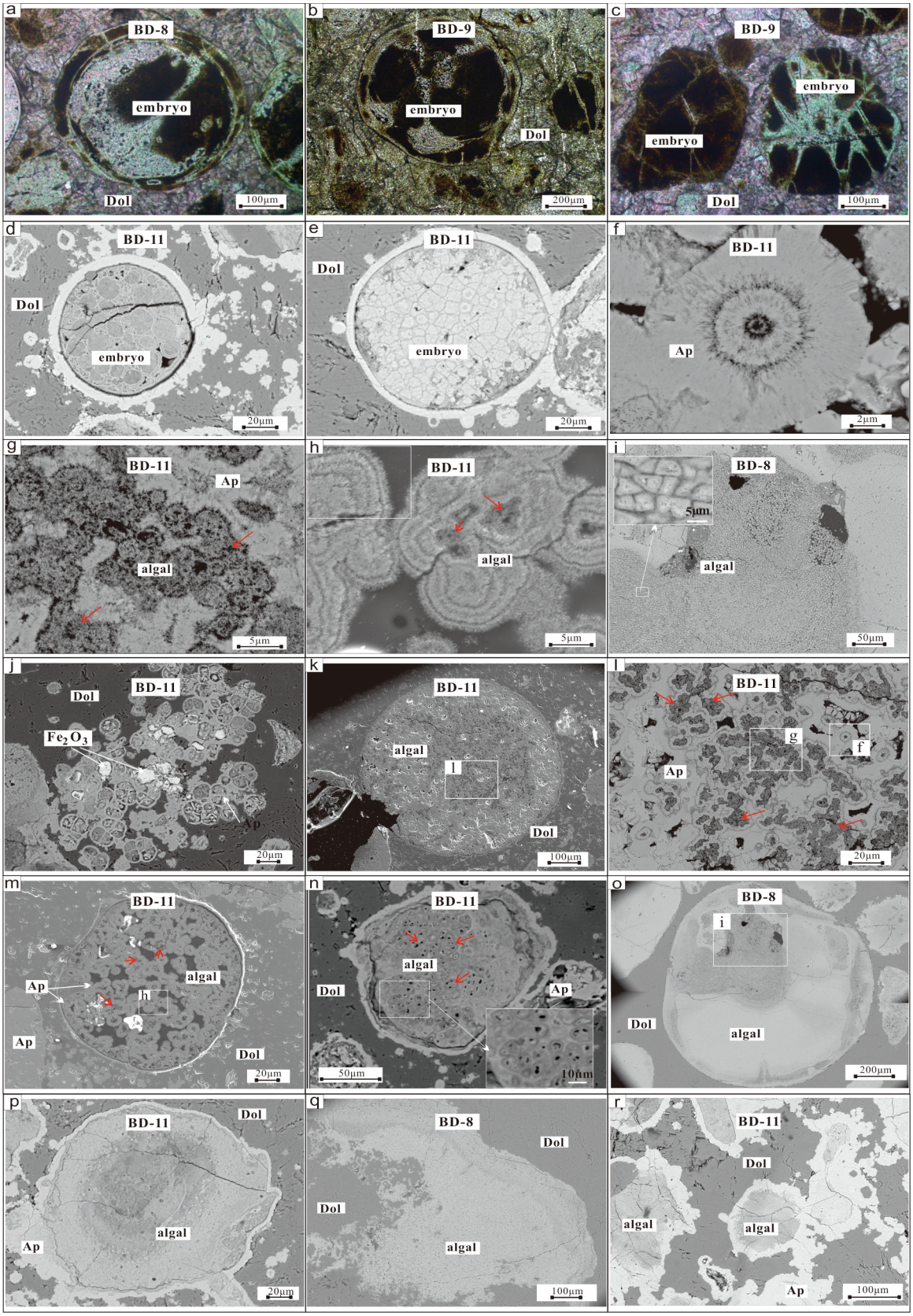

Fig. 8. Microstructures of microbial phosphate of the Doushantuo Formation phosphorites (a, b, and c are under transmitted light and plane polarized, d – j, l, and n – r are backscattered electron images, k and m are secondary electron images). (a, b, c, d and e) animal embryos containing two-cell texture (a), four-cell texture (b) and closely packed multi-cell texture (c, d, e); (f) concentric texture; (g) pistil-like texture; (h) irregularly concentric texture; (i) cell-stacked texture; (j) petaloid apatite; (k – o) aggregated algae. (f and g) magnified views of the square in (l); (l) magnified views of the square in (k); (i) magnified views of the square in (o); (p) concentrically zoned granules; (q) damaged algae-like microfossils; (r) amorphous apatite serving as cement. BD represents the Baidou ore block, Ap represents apatite, Dol represents dolomite, and Qtz represents quartz.

Table 2
Results of electron microprobe analyses (EMPA) of phosphorites from the Baidou ore block in Weng'an and the Jinzhong ore block in Kaiyang, Doushantuo Formation, Ediacara (wt%).

Number/element	Phosphate type	F	P_2O_5	CaO	MgO	SiO_2	MnO	Al_2O_3	SO_3	La_2O_3	Ce_2O_3	Pr_2O_3	ThO_2	Nd_2O_3	Total content
BD-1-1-2	Intraclast	4.27	39.46	53.70	0.20	0.52	0.00	0.30	0.63	0.04	0.00	0.00	0.05	0.02	99.18
BD-1-1-3		4.02	39.97	53.78	0.19	0.03	0.02	0.00	0.63	0.00	0.00	0.00	0.00	0.01	98.64
BD-1-2-1		3.55	40.24	51.44	0.21	0.09	0.01	0.01	0.62	0.00	0.00	0.01	0.01	0.01	98.64
BD-1-2-2		3.76	39.48	52.90	0.19	0.34	0.04	0.20	0.61	0.04	0.02	0.00	0.00	0.01	97.60
BD-1-2-4		3.90	38.90	53.33	0.19	0.49	0.02	0.24	0.68	0.06	0.00	0.01	0.05	0.05	97.90
BD-1-3-1		3.96	39.59	53.45	0.21	0.27	0.03	0.02	0.68	0.01	0.00	0.00	0.01	0.03	98.27
BD-1-3-2		3.77	40.12	53.49	0.27	0.19	0.02	0.00	0.69	0.01	0.04	0.00	0.04	0.00	98.63
BD-1-4-1		3.81	40.00	53.36	0.03	1.50	0.00	0.33	0.59	0.00	0.02	0.02	0.00	0.00	96.65
BD-1-4-2		4.41	39.69	53.46	0.04	0.05	0.03	0.02	0.62	0.00	0.06	0.00	0.00	0.00	98.36
BD-1-4-3		4.52	40.79	53.24	0.20	0.02	0.08	0.01	0.61	0.00	0.06	0.00	0.01	0.08	99.61
BD-1-5-1		3.74	40.56	54.13	0.18	0.10	0.04	0.00	0.64	0.00	0.06	0.00	0.00	0.00	99.45
BD-1-5-2		4.07	40.71	52.50	0.03	0.04	0.02	0.03	0.57	0.01	0.05	0.02	0.04	0.01	98.09
BD-3-1-1	Intraclast	4.09	40.41	53.67	0.04	0.19	0.03	0.02	0.59	0.00	0.00	0.00	0.03	0.01	99.07
BD-3-1-3		4.71	40.15	54.21	0.14	0.44	0.03	0.18	0.64	0.02	0.00	0.02	0.00	0.00	100.54
BD-3-2-1		4.29	39.35	53.75	0.02	0.68	0.01	0.19	0.64	0.01	0.10	0.00	0.00	0.04	99.17
BD-3-2-2		3.82	39.67	53.72	0.21	0.61	0.00	0.18	0.54	0.05	0.00	0.00	0.04	0.04	98.89
BD-3-3-1		4.11	39.90	54.41	0.17	0.12	0.03	0.00	0.56	0.02	0.00	0.02	0.00	0.00	99.34
BD-3-3-2		4.24	39.74	54.24	0.20	0.32	0.33	0.00	0.62	0.06	0.00	0.00	0.00	0.00	99.46
BD-3-4-1		4.28	39.16	54.53	0.16	0.52	0.01	0.19	0.67	0.00	0.04	0.00	0.00	0.00	99.56
BD-3-4-2		4.13	39.97	54.26	0.03	0.09	0.04	0.00	0.63	0.03	0.02	0.00	0.05	0.04	99.29
BD-4-2-1	Intraclast	3.86	41.29	53.92	0.03	0.01	0.00	0.00	0.53	0.00	0.00	0.00	0.01	0.03	99.68
BD-4-2-2		4.31	39.40	53.59	0.17	0.36	0.04	0.16	0.74	0.04	0.01	0.00	0.05	0.04	98.90
BD-4-2-3		4.00	36.93	49.71	0.47	4.46	0.01	1.88	0.67	0.02	0.03	0.00	0.04	0.04	98.27
BD-4-3-1		3.90	39.49	53.99	0.29	0.72	0.04	0.38	0.65	0.00	0.04	0.03	0.01	0.00	99.52
BD-4-3-2		3.58	36.64	48.57	0.41	6.90	0.00	2.38	0.58	0.04	0.00	0.01	0.05	0.00	99.15
BD-4-3-3		3.45	36.77	49.29	0.36	6.42	0.05	2.86	0.60	0.01	0.00	0.00	0.00	0.00	99.80
BD-4-4-1		4.81	39.19	53.39	0.02	0.67	0.02	0.14	0.65	0.03	0.06	0.00	0.02	0.01	99.01
BD-4-4-2		4.00	38.72	53.81	0.04	2.93	0.08	0.70	0.60	0.00	0.00	0.01	0.00	0.00	100.87
BD-4-4-3		3.98	37.47	49.54	0.24	9.41	0.07	1.18	0.70	0.00	0.00	0.01	0.00	0.02	102.62

Number/element	Phosphate type	F	P_2O_5	CaO	MgO	SiO_2	MnO	Al_2O_3	SO_3	La_2O_3	Ce_2O_3	Pr_2O_3	ThO_2	Nd_2O_3	Total content
BD-4-4-4	Intraclast	4.10	40.17	54.15	0.29	0.44	0.05	0.26	0.59	0.00	0.00	0.02	0.04	0.03	100.13
BD-6-1-1		3.65	41.07	53.48	0.20	0.00	0.00	0.00	0.53	0.00	0.00	0.00	0.01	0.00	98.93
BD-6-2-1		3.26	40.04	53.22	0.24	0.02	0.00	0.00	0.74	0.00	0.07	0.01	0.00	0.00	97.59
BD-6-3-1		3.08	41.06	53.28	0.21	0.02	0.01	0.00	0.67	0.01	0.00	0.00	0.00	0.00	98.35
BD-6-4-1		3.30	39.91	53.47	0.24	0.00	0.00	0.00	0.67	0.02	0.06	0.00	0.03	0.00	97.71
BD-6-5-1		3.13	40.59	53.97	0.19	0.03	0.02	0.00	0.74	0.00	0.00	0.02	0.00	0.01	98.78
BD-8-2-3	Microbial	3.17	40.77	54.89	0.03	0.03	0.01	0.01	0.45	0.01	0.05	0.01	0.00	0.01	99.44
BD-8-3-1		2.77	41.28	54.65	0.14	0.03	0.02	0.00	0.51	0.00	0.00	0.00	0.03	0.04	99.46
BD-8-4-1		3.33	41.15	53.10	0.02	0.01	0.02	0.01	0.67	0.08	0.00	0.01	0.04	0.01	98.45
BD-8-4-2		3.81	40.49	54.45	0.02	0.01	0.01	0.02	0.56	0.00	0.10	0.00	0.00	0.00	99.47
BD-10-1-1	Microbial	4.13	40.22	53.19	0.20	0.03	0.01	0.00	0.52	0.02	0.08	0.00	0.01	0.00	98.42
BD-10-2-1		3.37	41.07	52.60	0.20	0.01	0.00	0.00	0.58	0.00	0.02	0.00	0.04	0.00	99.15
BD-10-3-2		3.73	39.70	51.32	0.30	1.66	0.01	1.11	0.53	0.00	0.01	0.01	0.00	0.03	98.41
BD-10-4-1		3.86	41.29	53.92	0.03	0.01	0.00	0.01	0.53	0.00	0.00	0.00	0.01	0.03	99.68
BD-10-5-1		3.63	41.46	53.52	0.23	0.18	0.00	0.14	0.48	0.05	0.00	0.01	0.04	0.06	99.81
BD-10-5-2		3.38	40.44	50.04	0.04	0.00	0.03	0.00	0.46	0.04	0.00	0.00	0.05	0.11	97.58
BD-10-5-4		3.81	40.58	54.31	0.03	0.00	0.01	0.00	0.49	0.04	0.01	0.00	0.03	0.01	99.32
BD-10-5-6		3.78	40.73	53.96	0.04	0.00	0.02	0.00	0.51	0.00	0.02	0.00	0.00	0.00	99.05
BD-11-1-1	Microbial														
bial	4.09	40.64	53.92	0.01	0.00	0.04	0.00	0.64	0.01	0.00	0.00	0.01	0.00	99.35	
BD-11-3-1		4.10	44.01	55.24	0.01	0.00	0.00	0.00	0.01	0.02	0.00	0.02	0.01	0.00	103.42
BD-11-3-2		3.65	43.28	54.58	0.03	0.07	0.00	0.00	0.35	0.04	0.04	0.00	0.00	0.02	102.07
BD-12-2-1	Micro-bial	4.02	41.48	55.64	0.01	0.04	0.02	0.00	0.42	0.00	0.00	0.01	0.00	0.03	101.67
BD-12-3-1		4.08	41.43	55.69	0.00	0.00	0.01	0.01	0.51	0.00	0.00	0.00	0.05	0.00	101.79
BD-12-4-1		3.93	41.53	55.14	0.01	0.01	0.00	0.00	0.44	0.00	0.00	0.00	0.00	0.00	101.06
JZ-1-1-1	Intraclast	4.13	40.68	53.38	0.02	0.25	0.09	0.14	0.46	0.00	0.00	0.00	0.47	0.00	99.19
JZ-1-1-2		3.99	39.79	53.77	0.00	0.50	0.08	0.24	0.47	0.02	0.01	0.00	0.00	0.01	98.86
JZ-1-2-1		3.58	40.66	54.55	0.02	0.02	0.07	0.00	0.43	0.02	0.00	0.01	0.05	0.06	99.47
JZ-1-2-2		3.89	40.80	52.85	0.00	0.06	0.05	0.01	0.46	0.00	0.00	0.00	0.00	0.04	98.16
JZ-1-3-1		3.99	39.95	51.73	0.01	1.32	0.05	0.48	0.43	0.00	0.00	0.00	0.00	0.00	97.98

Number/element	Phosphate type	F	P_2O_5	CaO	MgO	SiO_2	MnO	Al_2O_3	SO_3	La_2O_3	Ce_2O_3	Pr_2O_3	ThO_2	Nd_2O_3	Total content
Z-1-3-3	Intraclast	3.87	40.24	54.10	0.02	0.14	0.05	0.00	0.36	0.00	0.00	0.00	0.06	0.00	98.84
JZ-1-3-4		4.15	38.95	50.75	0.02	3.08	0.07	1.52	0.40	0.00	0.00	0.00	0.00	0.02	98.96
JZ-1-3-5		4.38	40.59	54.97	0.00	0.05	0.10	0.03	0.48	0.01	0.00	0.03	0.00	0.00	100.63
JZ-1-4-1		3.99	38.21	51.06	0.30	3.11	0.03	1.21	0.37	0.01	0.01	0.00	0.00	0.06	98.36
JZ-2-1-1	Intraclast	3.92	40.88	55.06	0.00	0.05	0.13	0.01	0.47	0.04	0.04	0.02	0.03	0.00	100.65
JZ-2-2-1		3.91	40.75	54.31	0.01	0.06	0.06	0.00	0.41	0.00	0.00	0.00	0.02	0.05	99.57
JZ-2-2-2		4.11	40.92	55.02	0.01	0.04	0.04	0.01	0.49	0.01	0.07	0.01	0.00	0.00	100.71
JZ-2-3-1		4.17	39.86	53.83	0.01	0.63	0.04	0.29	0.48	0.00	0.00	0.01	0.00	0.01	99.28

(*continued on next page*)

Table 2 (*continued*)

Number/element	Phosphate type	F	P_2O_5	CaO	MgO	SiO_2	MnO	Al_2O_3	SO_3	La_2O_3	Ce_2O_3	Pr_2O_3	ThO_2	Nd_2O_3	Total content
JZ-2-3-3		3.40	39.96	52.47	0.22	2.29	0.01	0.93	0.32	0.01	0.02	0.01	0.03	0.00	99.67
JZ-2-4-1		3.86	40.52	53.17	0.03	1.68	0.05	0.64	0.40	0.00	0.00	0.02	0.00	0.03	100.39
JZ-2-4-2		3.37	39.87	52.40	0.03	2.40	0.06	0.90	0.46	0.01	0.00	0.00	0.00	0.02	99.51
JZ-3-1-1	Intraclast	3.57	39.41	53.55	0.02	0.30	0.10	0.21	0.52	0.03	0.00	0.02	0.07	0.03	97.83
JZ-3-2-1		3.96	40.75	54.94	0.02	0.33	0.08	0.17	0.41	0.05	0.01	0.00	0.00	0.03	100.74
JZ-3-3-1		3.87	41.77	55.17	0.00	0.27	0.07	0.18	0.67	0.00	0.00	0.00	0.04	0.00	102.05
JZ-3-3-2		3.54	39.70	55.60	0.01	0.07	0.09	0.00	0.49	0.00	0.10	0.00	0.03	0.02	99.65
JZ-3-4-1		4.10	40.10	54.03	0.00	0.04	0.10	0.00	0.55	0.04	0.00	0.00	0.00	0.01	99.97
JZ-4-1-1	Intraclast	3.69	41.57	54.49	0.03	0.00	0.01	0.01	0.59	0.03	0.03	0.00	0.00	0.01	100.44
JZ-4-2-1		4.22	41.13	52.98	0.03	0.01	0.07	0.00	0.47	0.01	0.00	0.00	0.02	0.01	98.96
JZ-4-3-1		3.89	41.28	54.51	0.01	0.00	0.05	0.00	0.53	0.02	0.00	0.01	0.00	0.03	100.33
JZ-4-3-2		4.04	41.84	54.22	0.02	0.04	0.05	0.01	0.59	0.00	0.00	0.00	0.01	0.00	100.81
JZ-4-4-1		3.76	41.61	54.77	0.13	0.02	0.05	0.01	0.59	0.01	0.01	0.02	0.00	0.01	100.99
JZ-5-1-1	Intraclast	3.86	40.20	52.92	0.23	0.32	0.00	0.21	0.67	0.00	0.00	0.00	0.00	0.01	98.42
JZ-5-2-1		4.00	41.60	54.73	0.04	0.03	0.01	0.00	0.61	0.00	0.00	0.00	0.00	0.00	101.03
JZ-5-3-1		4.03	41.16	52.53	0.01	0.07	0.09	0.01	0.55	0.02	0.00	0.00	0.00	0.02	98.48
JZ-5-4-1		4.29	41.13	54.05	0.02	0.25	0.01	0.12	0.63	0.05	0.10	0.00	0.04	0.00	100.68
JZ-5-5-1		4.96	40.42	50.81	0.22	0.32	0.04	0.28	0.63	0.00	0.01	0.01	0.00	0.00	100.69
JZ-5-5-2		3.93	40.71	53.77	0.00	0.17	0.38	0.02	0.08	0.02	0.08	0.00	0.04	0.00	99.16
Average value		3.84	40.48	53.66	0.10	0.48	0.04	0.18	0.54	0.01	0.02	0.01	0.02	0.01	99.49

the Ca, P, O, and F contents of the gray annuli are much higher than those of the dark-gray annuli, and the element contents show coordinated variations, indicating the periodic change in metallogenic material concentrations during formation.

5.3. Bulk rock geochemistry

5.3.1. Major elements

The major element compositions of the Doushantuo samples are listed in Table 1. The P_2O_5 content of layer A range from 10.99 to 38.25%, with an average of 32.31%; the F content range from 1.2 to 3.8%, with an average of 3.1%; the CaO content vary from 16.71 to 52.66%, with an average of 45.60; the MgO content vary from 0.13 to 3.26%, with an average of 1.04%; the SiO_2 content vary from 2.14 to 43.0%, with an average of 9.28% and the Al_2O_3 content vary from 0.21 to 12.05%, with an average of 2.17%. The P_2O_5 content of layer B range from 11.35 to 39.40%, with an average of 28.7%; the F content range from 1.1 to 3.7%, with an average of 2.8%; the CaO content vary from 36.81 to 53.87%, with an average of 46.89%; the MgO content vary from 0.12 to 14.75%, with an average of 5.44%; the SiO_2 content vary from 0.5 to 11.35%, with an average of 1.99% and the Al_2O_3 content vary from 0.06 to 0.47%, with an average of 0.27%. In summary, the samples from layer B exhibit lower P_2O_5 grades (28.70%) and F contents (2.8%) than layer A do (32.31% and 3.1%, respectively), suggesting that the deposits are middle–high–grade phosphorites. The wall rocks are richer in MgO (10.2%) and SiO_2 (35.94%) and exhibit a higher LOI (22.34%), whereas they are depleted in F, P_2O_5 (6.63%), and CaO (23.35%) compared with the phosphorites.

The Doushantuo phosphorites were divided into four types, and the average P_2O_5 and F contents of each phosphorite type are as follows: grainy phosphorite (P_2O_5 = 35.75% and F = 3.42%) > biological phosphorite (P_2O_5 = 22.95% and F = 2.25%) > cataclastic phosphorite (P_2O_5 = 20.87% and F = 1.90%) > phosphatic detritus (P_2O_5 = 10.99% and F = 1.2%). The major elements show that the Doushantuo phosphorites consist of F-bearing phosphate minerals, and the wall rocks are siliceous dolostones.

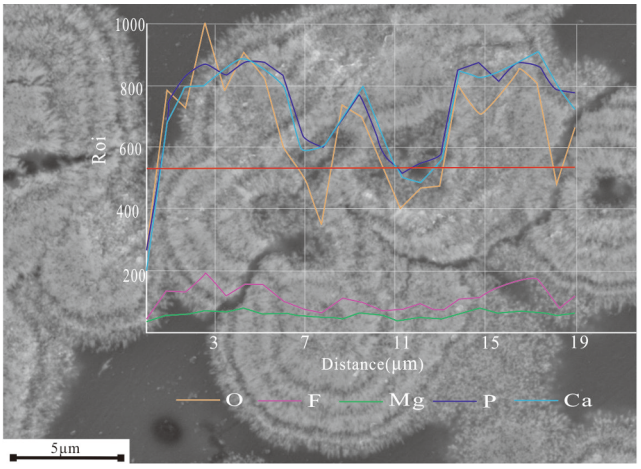

Fig. 10. Energy spectrum line analysis of partial major elements of irregularly concentric apatite. The image is a back-scattered electron (BSE) image.

The major element correlations of phosphorite (Table 3, Fig. 11) show that P_2O_5 have a significantly positive correlation with CaO and F but a slightly negative correlation with MgO, SiO_2, Al_2O_3, and TiO_2; the correlation coefficients are as follows: P_2O_5–CaO = 0.90, P_2O_5–F = 0.97, P_2O_5–MgO = –0.84, P_2O_5–SiO_2 = –0.54, P_2O_5–Al_2O_3 = –0.37, and P_2O_5–TiO_2 = –0.40. In addition, the correlation coefficients of some major

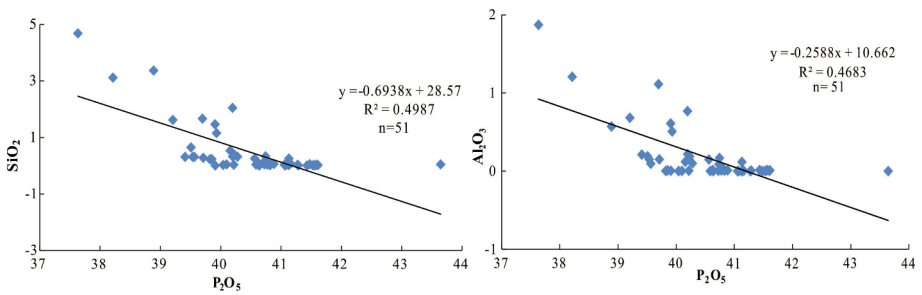

Fig. 9. Correlation diagrams for the major elements of collophane in Weng'an (Baidou) and Kaiyang (Jinzhong) derived from EMPA.

Table 3
Correlations of major elements in bulk rock samples from the Doushantuo Formation of Central Guizhou ($R > 0.5$ and $R < 0.5$ represent a positive relationship and negative relationship, respectively; $-0.5 < R < 0.5$ represents no detectable correlation between two elements). The value representing obvious correlation (both negative and postive) were bold in the table.

	Al_2O_3	CaO	F	TFe_2O_3	MgO	P	SiO_2	LOI
Al_2O_3	1.00							
CaO	−0.70	1.00						
F	−0.22	**0.77**	1.00					
TFe_2O_3	**0.60**	−0.33	0.08	1.00				
MgO	−0.14	**−0.52**	**−0.89**	−0.29	1.00			
P	−0.37	**0.90**	**0.94**	−0.05	**−0.84**	1.00		
SiO_2	**0.84**	**−0.84**	−0.36	**0.50**	0.00	**−0.54**	1.00	
LOI	−0.13	**−0.53**	**−0.89**	−0.31	1.00	**−0.84**	0.01	1.00

elements are as follows: Al_2O_3–TFe_2O_3 = 0.6, Al_2O_3–SiO_2 = 0.84, and CaO–F = 0.77, showing significantly positive correlations; CaO–MgO = –0.52, CaO–SiO_2 = –0.84, and F–MgO = –0.89, showing significantly negative correlations.

5.3.2. Trace elements

The trace element compositions of the Doushantuo phosphorites and wall rocks are listed in Table 4. The PAAS - normalized distributions for partial trace elements of layers A and B are almost identical (Fig. 12). All samples are enriched with Sr and U, with enrichment coefficients of 1.09–5.65 (average = 3.97) and 0.85–4.74 (average = 3.06), respectively (Fig. 12a–e). Additionally, Yingping phosphorites are enriched with Zn, and the enrichment coefficient is 1.78–5.40, with an average of 2.20. The partial phosphorites of Baidou and Wenquan are enriched with Co, Ba, and Pb, with enrichment coefficients of 0.43–2.83 (average = 1.19), 17–6.83 (average = 1.89), and 0.83–2.16 (average = 1.39), respectively (Table 4). The wall rocks are rich in Co and Th and depleted in Cu when compared with PAAS (Fig. 12f). Doushantuo phosphorites are much richer in Ba, As, and Sr compared with the values of the bulk continental crust (Taylor and Mclennan, 1985) and average carbonatites (Liu and Cao, 1987) and are richer in Co and Ba than modern marine phosphorites (Baturin, 1981), while the wall rocks are richer in Co and As (Table 5).

In this study, RSE indices, such as V/Sc, V/Cr, Ni/Co, V/(Vr + Ni), δU, and Th/U, were used to determine the redox environment (Table 4). Differences in the RSE indices between layers A and B are

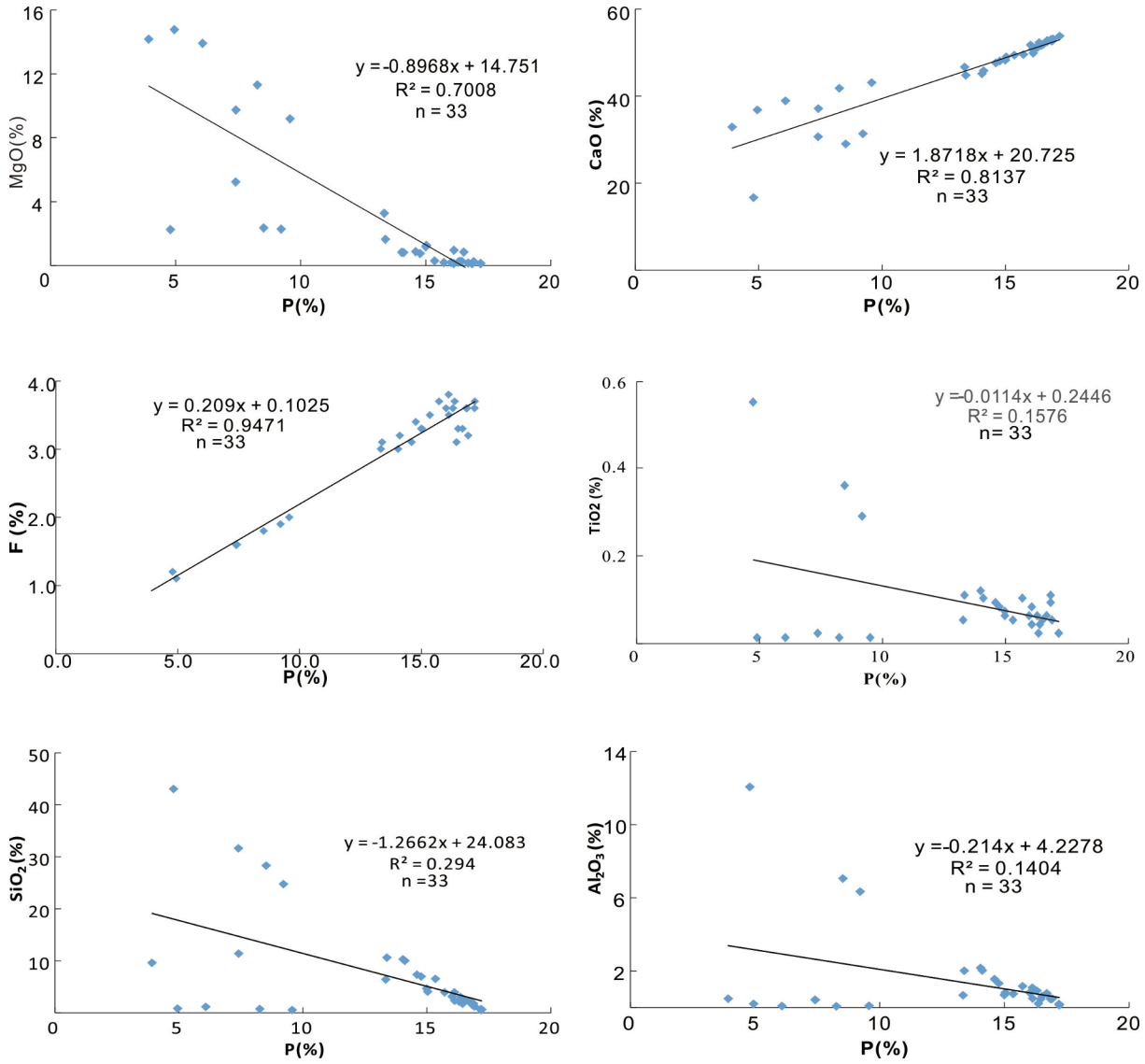

Fig. 11. Correlation diagrams for the major elements of phosphorite in Central Guizhou, Ediacaran Doushantuo Formation. *R* represents the correlation coefficient, and *n* represents the number of samples.

Table 4
Trace element analyses of phosphorites from Central Guizhou, Doushantuo Formation, Ediacara (ppm).

	Li	Be	Sc	V	Cr	Co	Ni	Cu	Zn	Ga	Ge	As	Rb	Sr	Y	Zr	Nb	Mo	Ag	
BD-1	5.47	2.98	3.63	17.10	10.70	58.60	9.25	3.62	3.60	3.57	0.23	7.92	13.90	1040.00	62.20	42.80	2.03	0.41	0.13	
BD-2	6.31	3.78	2.53	14.50	9.73	27.50	8.24	3.39	2.27	3.50	0.30	6.96	13.20	1050.00	65.80	43.60	1.90	0.30	0.08	
BD-3	5.20	2.42	1.66	13.30	5.96	25.80	7.89	3.56	1.67	2.83	0.29	6.16	9.16	1010.00	80.80	39.10	1.59	0.30	0.11	
BD-4	5.32	3.37	1.99	13.00	7.31	13.20	6.98	0.98	2.27	3.33	0.30	4.72	11.00	1060.00	75.10	42.30	1.76	0.28	0.04	
BD-6	1.75	2.53	2.10	13.50	14.00	15.80	12.80	12.10	15.40	1.73	0.11	49.01	1.99	1130.00	51.10	16.90	0.49	0.92	0.89	
BD-7	1.80	1.50	0.48	40.40	18.80	18.10	10.00	5.89	52.40	1.78	0.11	10.95	2.43	1030.00	43.80	14.90	0.65	0.28	0.07	
BD-8	1.15	0.50	0.51	21.10	5.04	14.00	6.99	3.37	21.70	0.66	0.06	5.79	0.57	321.00	3.73	2.73	0.13	0.39	0.03	
BD-9	1.24	0.45	0.54	12.20	4.10	35.70	8.42	4.29	11.30	0.78	0.05	3.77	0.32	460.00	3.69	2.64	0.08	0.39	0.03	
BD-10	1.44	1.60	0.85	15.40	3.62	22.60	8.85	2.76	26.50	0.93	0.10	5.83	0.58	743.00	10.10	5.28	0.14	0.16	0.03	
BD-11	0.69	0.77	1.73	9.01	7.82	6.99	6.39	3.10	76.30	0.73	0.07	4.86	1.11	251.00	31.00	4.61	0.23	0.14	0.05	
BD-12	2.15	0.09	1.53	25.70	12.10	20.30	7.02	2.42	20.00	1.32	0.15	3.91	2.65	218.00	27.20	10.10	0.52	0.16	0.15	
CD-1	37.20	2.60	8.76	74.40	44.60	19.60	8.97	26.40	16.10	14.90	2.84	196.22	66.30	994.00	49.90	119.00	8.63	1.04	0.36	
CD-2	15.70	2.91	6.70	57.80	30.90	18.70	19.10	15.30	13.60	10.00	1.51	70.57	44.20	826.00	57.10	93.20	5.86	1.54	0.24	
CD-3	5.05	4.92	6.03	41.10	24.70	21.60	18.80	11.70	11.20	8.61	0.70	51.46	45.90	641.00	51.90	72.90	4.80	0.81	0.17	
CD-4	3.96	4.53	3.88	22.80	11.40	16.60	12.40	5.38	6.49	4.02	0.38	14.91	15.30	917.00	75.10	57.20	2.47	0.59	0.14	
JZ-1	10.80	1.48	2.69	13.60	6.04	10.60	10.50	2.62	4.31	3.79	0.47	32.25	5.68	779.00	158.00	55.10	2.22	0.87	0.08	
JZ-2	12.30	1.71	3.51	17.80	8.12	12.60	13.10	4.59	14.10	4.13	0.49	52.80	7.24	837.00	129.00	57.10	2.47	0.53	0.11	
JZ-3	8.18	1.30	3.10	14.40	6.90	9.62	11.00	3.55	8.00	3.44	0.39	24.51	4.77	767.00	122.00	48.00	1.92	0.62	0.10	
JZ-4	8.94	1.79	3.27	16.00	5.31	11.20	12.20	11.60	15.80	2.56	0.30	8.59	3.71	816.00	59.40	59.40	1.51	0.40	0.07	
JZ-5	7.89	0.68	1.36	26.30	8.79	81.50	27.10	154.00	94.80	2.61	0.39	23.75	5.03	801.00	33.20	52.90	1.40	1.70	0.18	
YP-1	7.38	1.80	2.03	34.60	6.34	16.30	15.30	15.20	270.00	3.22	0.31	54.40	5.87	731.00	62.00	32.60	1.39	0.55	0.08	
YP-4	1.08	1.46	0.51	5.51	3.82	13.40	12.10	1.73	89.70	1.49	0.09	4.47	0.46	869.00	20.20	4.20	0.18	0.20	0.02	
YP-5	1.58	1.26	0.31	7.18	5.15	10.10	10.90	2.05	139.00	1.44	0.07	4.37	0.69	804.00	27.00	7.22	0.23	0.12	0.04	
YP-6	1.03	1.56	1.08	14.40	18.10	23.70	15.10	5.27	89.90	2.01	0.11	9.10	2.47	824.00	25.90	90.40	1.46	0.27	0.07	
YP-7	1.16	0.75	0.74	14.60	14.10	9.51	12.50	5.67	90.70	2.04	0.17	13.39	2.53	667.00	32.40	60.80	1.26	0.19	0.10	
WQ-1	7.92	1.60	3.20	23.70	6.88	24.50	13.90	73.40	9.08	2.78	0.39	37.56	5.49	945.00	72.40	36.30	1.51	1.80	0.11	
WQ-2	2.67	1.08	0.89	19.20	4.79	38.40	17.60	43.60	8.02	2.34	0.24	37.05	4.61	1000.00	27.00	49.20	1.39	2.58	0.25	
WQ-3	3.27	1.77	0.92	14.50	5.26	60.80	15.30	56.90	7.29	2.60	0.19	46.49	5.76	909.00	27.40	55.60	1.71	2.36	0.30	
WQ-4	1.66	0.39	0.82	19.10	3.88	65.00	18.70	71.60	6.74	2.19	0.17	53.14	3.90	981.00	18.20	42.80	1.19	2.40	0.28	
WQ-5	10.00	0.80	0.06	12.50	2.57	23.20	13.00	42.30	22.30	1.78	0.18	23.58	1.62	895.00	11.20	6.63	0.41	0.58	0.14	
WQ-6	1.72	0.61	1.13	16.10	9.96	11.90	15.00	69.60	6.65	2.91	0.27	29.73	5.07	1050.00	70.60	44.60	1.50	0.93	0.19	
BD-5	2.69	1.02	0.42	14.90	4.31	9.82	5.84	4.37	8.77	1.37	0.10	12.97	3.25	280.00	23.80	16.00	0.74	0.07	0.07	
JZ-6	0.60	0.45	1.25	2.75	3.61	22.10	6.98	4.88	14.50	0.13	0.05	2.03	0.03	40.80	1.01	1.78	0.05	0.09	0.03	
YP-2	3.48	0.32	1.50	12.80	4.79	31.90	8.04	10.20	89.10	1.53	0.25	29.39	3.47	524.00	26.80	16.40	0.83	0.29	0.14	
YP-3	0.89	−0.06	−0.54	1.27	1.53	298.00	−0.29	0.35	0.00	0.12	0.22	0.67	0.21	4.90	0.06	0.60	0.02	0.28	0.03	

	Cd	In	Sn	Sb	Cs	Ba	Hf	Ta	W	Tl	Pb	Bi	Th	U	V/V + Ni	V/Cr	Th/U	δU	Ni/Co	V/Sc
BD-1	0.01	0.01	0.17	0.05	1.63	698.00	0.77	0.14	323.00	0.07	11.60	0.06	2.31	12.50	0.65	1.60	0.18	1.88	0.16	4.71
BD-2	−0.01	0.01	0.11	0.07	1.73	1690.00	0.76	0.16	201.00	0.06	12.10	0.07	2.35	13.30	0.64	1.49	0.18	1.89	0.30	5.72
BD-3	0.00	0.01	0.06	0.06	1.25	941.00	0.63	0.11	254.00	0.06	10.80	0.08	2.37	14.40	0.63	2.23	0.16	1.90	0.31	8.02
BD-4	−0.01	0.00	−0.05	0.03	1.39	3590.00	0.74	0.13	168.00	0.06	5.57	0.03	2.63	14.70	0.65	1.78	0.18	1.89	0.53	6.52
BD-6	0.12	0.00	−0.06	0.34	0.22	595.00	0.35	0.03	168.00	0.15	30.10	0.03	0.53	4.10	0.51	0.96	0.13	1.92	0.81	6.42
BD-7	0.07	0.00	−0.12	0.26	0.19	437.00	0.27	0.04	160.00	0.04	16.00	0.03	0.66	11.50	0.80	2.15	0.06	1.96	0.55	84.85
BD-8	0.10	0.00	−0.13	0.17	0.06	108.00	0.03	0.01	110.00	0.07	2.12	0.00	0.13	4.15	0.75	4.19	0.03	1.98	0.50	41.62
BD-9	0.08	0.00	−0.13	0.18	0.02	157.00	0.03	0.01	315.00	0.02	2.16	0.00	0.06	5.95	0.59	2.98	0.01	1.99	0.24	22.61
BD-10	0.08	0.00	−0.15	0.21	0.05	312.00	0.04	0.01	165.00	0.07	2.77	−0.01	0.16	6.03	0.64	4.25	0.03	1.98	0.39	18.11
BD-11	0.16	0.00	−0.10	0.21	0.07	110.00	0.16	0.02	56.10	0.01	2.37	0.01	0.29	2.63	0.59	1.15	0.11	1.93	0.91	5.19
BD-12	0.06	0.00	−0.08	0.18	0.23	99.50	0.18	0.03	140.00	0.03	2.36	0.00	0.96	4.72	0.79	2.12	0.20	1.87	0.35	16.75
CD-1	0.06	0.03	1.67	0.50	9.37	2540.00	3.09	0.63	147.00	0.19	33.60	0.14	7.85	8.42	0.89	1.67	0.93	1.53	0.46	8.50
CD-2	0.04	0.03	0.94	0.34	6.17	413.00	2.33	0.40	127.00	0.26	36.90	0.10	5.44	9.69	0.75	1.87	0.56	1.68	1.02	8.63
CD-3	0.01	0.02	0.70	0.13	5.90	530.00	1.82	0.35	139.00	0.27	32.60	0.10	4.31	8.13	0.69	1.66	0.53	1.70	0.87	6.82
CD-4	0.01	0.01	0.16	0.20	1.62	336.00	0.97	0.15	125.00	0.10	16.50	0.06	2.48	12.80	0.65	2.00	0.19	1.88	0.75	5.88
JZ-1	0.01	0.00	0.04	1.54	0.29	251.00	1.24	0.12	82.60	0.04	8.08	0.08	3.53	9.48	0.56	2.25	0.37	1.78	0.99	5.05

(*continued on next page*)

Table 4 (*continued*)

	Li	Be	Sc	V	Cr	Co	Ni	Cu	Zn	Ga	Ge	As	Rb	Sr	Y	Zr	Nb	Mo	Ag	
JZ-2	0.06	0.01	0.01	2.64	0.42	216.00	0.98	0.14	71.80	0.05	8.14	0.17	3.48	8.19	0.58	2.19	0.42	1.75	1.04	5.07
JZ-3	0.19	0.02	−0.03	1.70	0.25	250.00	0.83	0.08	74.80	0.04	5.86	0.08	4.25	7.46	0.57	2.09	0.57	1.68	1.14	4.64
JZ-4	0.10	0.01	−0.05	2.56	0.21	337.00	0.74	0.09	53.30	0.10	7.02	0.04	1.31	10.00	0.57	3.01	0.13	1.92	1.09	4.90
JZ-5	0.21	0.03	−0.05	6.36	0.29	603.00	0.84	0.06	143.00	1.29	15.90	0.37	1.09	10.90	0.49	2.99	0.10	1.94	0.33	19.35
YP-1	0.93	0.00	−0.02	2.60	0.27	429.00	0.58	0.06	120.00	0.10	13.60	0.06	0.91	12.20	0.69	5.46	0.07	1.95	0.94	17.08
YP-4	0.14	0.00	−0.13	0.48	0.01	644.00	0.10	0.01	133.00	0.06	3.80	0.02	0.14	7.80	0.31	1.44	0.02	1.99	0.90	10.85
YP-5	0.21	0.00	−0.13	0.47	0.02	600.00	0.12	0.02	86.00	0.02	4.89	0.00	0.19	7.83	0.40	1.39	0.02	1.98	1.08	22.84
YP-6	0.28	0.00	−0.06	1.42	0.09	689.00	1.99	0.10	198.00	0.05	13.60	0.02	1.64	6.25	0.49	0.80	0.26	1.84	0.64	13.28
YP-7	0.46	0.00	−0.10	1.55	0.10	546.00	1.46	0.07	75.10	0.05	7.58	0.01	1.62	5.97	0.54	1.04	0.27	1.83	1.31	19.65
WQ-1	0.03	0.02	0.00	1.64	0.54	2980.00	0.55	0.05	49.00	0.07	8.28	0.19	1.54	20.20	0.63	3.44	0.08	1.95	0.57	7.40
WQ-2	0.03	0.00	−0.01	0.56	0.36	4440.00	0.78	0.06	33.50	0.18	29.30	1.61	0.82	14.50	0.52	4.01	0.06	1.96	0.46	21.52
WQ-3	0.02	0.00	0.07	0.84	0.37	1370.00	0.86	0.08	65.30	0.23	20.30	1.54	1.08	12.90	0.49	2.76	0.08	1.95	0.25	15.81
WQ-4	0.02	0.00	0.05	1.29	0.42	3200.00	0.64	0.05	52.30	0.41	43.20	1.70	0.52	13.20	0.51	4.92	0.04	1.97	0.29	23.26
WQ-5	0.01	0.00	−0.10	1.60	0.08	219.00	0.09	0.02	84.00	0.02	17.20	0.22	0.12	9.50	0.49	4.86	0.01	1.99	0.56	205.92
WQ-6	0.03	0.00	0.12	2.18	0.87	1050.00	0.46	0.08	21.70	0.22	40.10	0.62	1.14	14.30	0.52	1.62	0.08	1.95	1.26	14.20
BD-5	0.03	0.00	−0.05	0.24	0.33	140.00	0.25	0.04	61.00	0.05	5.24	0.05	0.66	4.23	0.72	3.46	0.16	1.90	0.59	35.53
JZ-6	0.11	(0.00)	(0.17)	0.39	0.01	8.97	(0.01)	0.01	130.00	0.02	2.20	0.00	0.03	0.64	0.28	0.76	0.05	1.97	0.32	2.20
YP-2	0.22	0.01	−0.09	1.18	0.19	288.00	0.23	0.04	258.00	0.20	6.24	0.02	0.63	5.53	0.61	2.67	0.11	1.93	0.25	8.53
YP-3	0.00	0.00	−0.17	0.13	0.17	21.60	0.01	0.01	1470.00	0.00	−0.19	0.00	0.01	0.14	1.30	0.83	0.04	1.97	–	–

Annotation: δU = 6U/(3U + Th), according to Wignall (1991).

inconspicuous, so the RSE indices of layers A and B were discussed together. The V/Sc ratios range from 4.64 to 205.92, with an average of 20.94, and the Ni/Co ratios range from 0.16 to 1.31, with an average of 0.68. The V/Cr range from 0.80 to 5.46, with an average of 2.42, and the V/(Vr + Ni) ratios range from 0.311 to 0.89, with an average of 0.60 (Fig. 13a). The values of δU vary from 1.70 to 1.99, with an average of 1.88, and the Th/U ratios of phosphorite vary from 0.01 to 0.93, with an average of 0.2 (Fig. 13b). The wall rocks have similar ratios – δU (1.94), Th/U (0.09), V/Sc (13.97), V/Cr (2.25), Ni/Co (0.29), and V/(Vr + Ni) (0.73) – to those of phosphorites (Table 4). The Fe/Ti and Al/(Al + Fe + Mn) ratios of layer A are 2.98–63.29 (average = 18.46) and 0.14–0.80 (average = 0.48), whereas those of layer B are 2.92–18.67 (average = 7.75) and 0.27–0.70 (average = 0.47), respectively (Fig. 13c). The phosphorites and wall rocks both lay within the hydrothermal area in the lg[U]–lg[Th] diagram (Fig. 13d).

The contents of REEs and Y (ΣREE) and parameters of the Doushantuo phosphorite are shown in Table 6. The ΣREE presents a relatively large range of 28.29–507.58 ppm, with an average value of 158.51 ppm, which is lower than that of the PAAS (210.00 ppm). The ΣREE of the wall rocks are low, with an average of 38.64 ppm. The PAAS–normalized distributions for the REEs of layer B are characterized by the pronounced enrichment of middle REEs (MREEs) compared to those of both LREEs and HREEs, producing a “hat-shaped” REE plot (Fig. 14a and b); those of layer A show “left-inclining” REE plots (Fig. 14a and c–e), and the wall rocks show “flat-shaped” REE plots (Fig. 14f). The Ce_{anom} of the lower layer vary from –0.12 to –0.01, with an average of –0.07, whereas the Ce_{anom} of the upper layer vary from –0.32 to –0.23, with an average of –0.28 (Table 6). The $(Eu/Eu^*)_{SN}$ vary from 0.94 to 1.81, with an average of 1.11, showing moderately positive anomalies (Table 6). Furthermore, $(Ce/Ce^*)_{SN}$ show no correlation with ΣREE and Dy_N/Sm_N (Fig. 14 e and f; R–values are 0.20 and 0.08, respectively). Additionally, the chondrite–normalized REE distributions of phosphorites appeare to lie between hydrogenous and hydrothermal deposits (Fig. 15a, according to Oksuz (2011)). The North American shale composite (NASC)–normalized REE distributions of layer B show a “hat-shaped” REE plot, whereas those of layer A show a “left–inclining” REE plot (Fig. 15b), showing the same characteristics as PAAS–normalized REE distributions.

6. Discussion

6.1. Origin of metallogenic materials

In general, the Si, Al, and Ti contents represent the remains of terrestrial detrital matter, and the high Si, Al, and Ti contents indicate shallow waters close to the epicontinental area (Zhu et al., 2013) and the terrigenous source. In our study, the Al_2O_3, SiO_2, and TiO_2 contents throughtout the rock are much lower and show negative correlations with P_2O_5 (Fig. 11). Using EMPA, the Al_2O_3 and SiO_2 contents in the collophane are characterized by coordinated variation and show negative correlations with P_2O_5 (Fig. 9). These geochemical data indicate that the input of terrigenous materials into the Doushantuo phosphorite was limited.

Sverjensky (1984) suggested that the relative stabilities of aqueous Eu^{2+} and Eu^{3+} are closely associated with a wide range of temperatures, pressures, and Eh–pH conditions. Under high temperatures (> 250 °C) and elevated pressures, Eu^{3+} predominates, and the hydrothermal fluids and sediments formed under hydrothermal conditions are usually characterized by obvious positive Eu anomalies (Olivarez and Owen, 1991; Douville et al., 1999). Theoretically, Eu is oxidized to Eu^{3+} in oxic conditions and convert to Eu^{2+} in reducing conditions (Holser, 1997), presenting similar geochemical behaviors to other REEs under oxic conditions whereas separating from ther REEs under reducing conditions. Nevertheless, only under extremely reducing conditions could Eu^{2+} easily replace Ca^{2+} in phosphate, and thereby cause

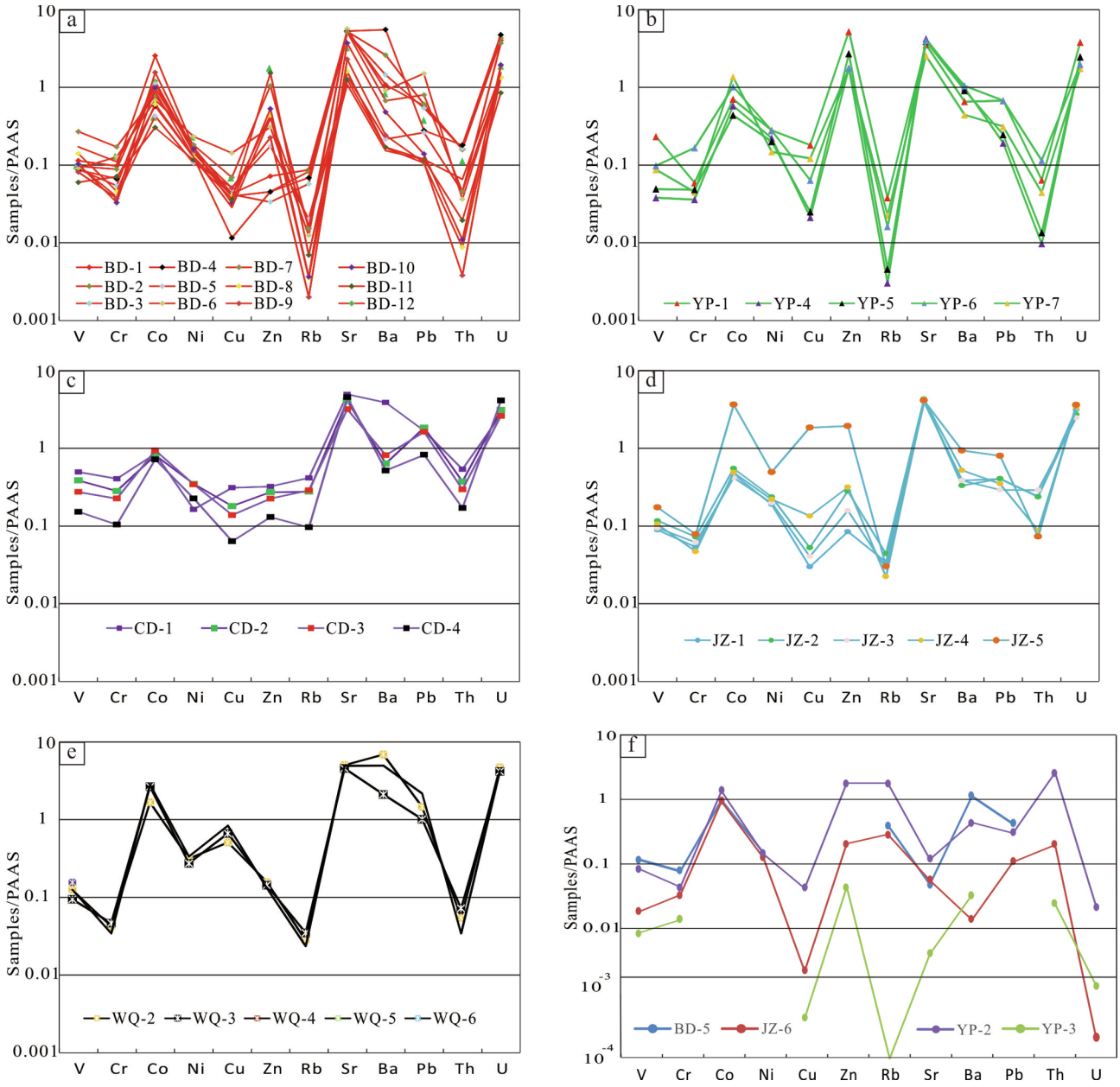

Fig. 12. The post–Archean Australian shale (PAAS)–normalized trace element distributions of phosphorites in the Ediacaran Central Guizhou Doushantuo Formation. The PAAS date accords to Taylor and Mclennan (1985). BD represents Baidou ore block, CD represents Chuangdong ore block, WQ represents Wenquan ore block, JZ represents Jingzhong ore block, YP represents Yingping ore block.

Table 5
Comparison of phosphorites in Central Guizhou between trace elements and some average data (ppm).

Sampling sites	V	Cr	Co	Ni	Zn	Cu	Ba	Pb	As	Sr
Baidou	17.51	8.62	22.37	8.22	20.18	4.15	739.79	8.60	10.24	716.08
Jinzhong	15.14	6.46	24.60	13.48	25.25	30.21	277.66	7.87	23.99	673.47
Yingping	12.91	7.69	57.56	10.52	109.77	5.78	459.66	7.07	16.54	631.99
Chuandong	49.03	27.90	19.13	14.82	11.85	14.70	954.75	29.90	83.29	844.50
Wenquan	17.52	5.56	37.30	15.58	10.01	59.57	2209.83	26.40	37.93	963.33
Average	21.32	10.54	24.43	12.43	37.33	21.55	980.02	14.98	28.97	818.26
Wall rocks	7.93	3.56	90.46	5.14	28.09	4.95	114.64	3.37	11.27	212.43
Bulk continental crust	230.00	185.00	29.00	105.00	80.00	75.00	250.00	8.00	1.0	260.00
Average carbonatite	20.00		0.10	20.00	20.00	4.00	100.00	9.00	1.00	610.00
Modern marine phosphorite	18.80		0.21	10.50	55.50	28.00	350.00		27.50	2800.00

Annotation: the dates of bulk continental crust is from Taylor and Mclennan (1985), the dates of average carbonatite is from Liu and Cao (1987), the dates of modern marine phosphorite is from (Baturin, 1981).

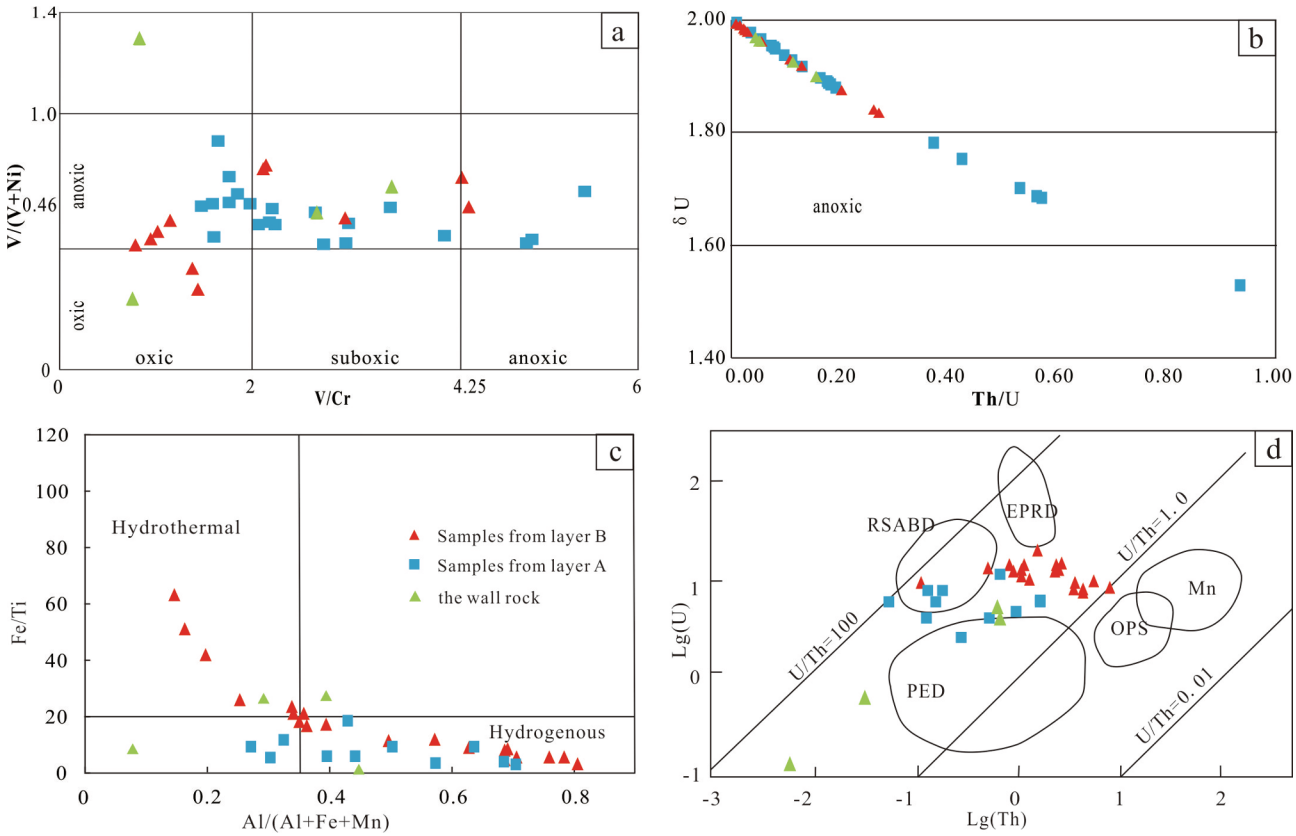

Fig. 13. Trace element discriminant diagrams of phosphorite in Central Guizhou, Ediacaran Doushantuo Formation. a: V/Cr–V/(V + Ni), V/Cr ratio is based on Jones and Manning (1994), V/(V + Ni) ratio is based on Yarincik et al. (2000); and b: δU–Th/U, δU is based on δU is based on Wignall (1991), Th/U ratio is based on Kimura and Watanabe (2001); c. Fe/Ti–Al/(Al + Fe + Mn), based on Yamamoto (1987); d. lg[U]–lg[Th] diagram, based on Boström (1983). Comment: EPRD: the east pacific ridge hydrothermal sediment area; RSABD: the Red Sea thermo-brine sedimentary area; Mn: manganese nodule area; OPS: pelagic sedimentary area; PED: petrochemical flow sediment area; ED: hydrothermal sediment area in the east pacific ridge; HN: hydrogenous sediment area; RH: the Red Sea hot brine sedimentary area; and HD: hydrothermal sediment area. (For interpretation of the references to colour in this figure legend, the reader is referred to the web version of this article.)

positive Eu anomalies (Baar et al., 1985). From our results, we suggest that the positive Eu anomalies are the result of hydrothermal activities rather than redox conditions because the positive Eu anomalies are recorded both in layer A (reducing conditions) and layer B (oxic conditions) (The redox conditions were discussed in detail in Section 6.2).

Other researches have shown that REEs are soluble in normal seawater, where the concentrations of LREEs are higher than those of HREEs, and LREEs enter sediments prior to HREEs (Goldberg et al., 1963; Henderson, 1984), resulting in a “right-inclining” REE plot in normal sediments. Moreover, under hydrothermal solutions, HREEs enter sediments prior to LREEs because of the lower stability of complex compounds (Henderson, 1984; Bau and Möller, 1992), resulting in a “left-inclining” REE plot (Marchig et al., 1982) in hydrothermal sediments. In general, the ΣREE is lower than 200 ppm in normal hydrogenetic sediments and higher than 200 ppm in hydrothermal sediments (Wang et al., 1989). Therefore, we suggest that the ΣREE of phosphorites record both hydrogenetic and hydrothermal characteristics. Dduring the formation of the phosphorites, hydrothermal fluids might have entered normal seawater according to the ΣREE, causing the “left-inclining” REE plot, especially in the earlier Doushantuo Formation (Fig. 14c–f).

Generally, the Th content is much higher than the U content in most sediment. In contrast, U content is higher than Th content in hydrothermal sediments because the sedimentation rate of U is faster under hydrothermal conditions, resulting in U enrichment. Research has shown a U/Th ratio > 1 indicates hydrothermal sedimentation and that of < 1 indicates normal hydrogenous sedimentation (Rona et al., 1984). Further research has suggested that hydrothermal sediments are rich in Fe and Mn, but lack Cu, Co, and Ni, whereas Al and Ti are generally derived from terrigenous materials (Boström, 1983; Zhou, 1990). Hence, Al/(Al + Fe + Mn) values of less than 0.35 and Fe/Ti values of more than 20 (Yamamoto, 1987) are considered as resulting from hydrothermal processes. The Fe/Ti–Al/(Al + Fe + Mn) (Fig. 13c) and lg[U]–lg[Th] diagrams (Fig. 13d) indicate that hydrotherm al activities participated in the formation of phosphorites.

The Eu anomalies, Fe/Ti, Al/(Al + Fe + Mn), lg[U]–lg[Th] diagram, chondrite–normalized and NASC–normalized REE distributions of phosphorites revealed that hydrothermal activities might have played an important role in providing, carrying, and precipitating P in Doushantuo phosphorites. These activities were part of the phosphogenic events along with the cycles of marine transgressions and regressions. So, we suggest that the hydrothermal processes, along with normal seawater might have contributed to the metallogenic materials, which is consistent with the paleogeography. The plate tension of the Yangtze Platform in the Cryogenian Period caused basins to rift, which developed a series of graben–horst structures and deep fractures along with intense volcanic activities, such as explosive volcanism and magmatic eruptions (Liu et al., 1993; Jiang et al., 2003). During the deposition of the Doushantuo Formation in the Ediacaran, the Yangtze Platform inherited the earlier paleotectonic basins and provided a space conducive to deposition, even though volcanic activities had noticeably declined (Liu, 1987). Seawater that infiltrated along the faults was transformed into hydrothermal fluids and heated in the lower parts of faults before injection into the bottom seawater. Under these circumstances, the mingling of hydrothermal fluids and normal seawater provided metallogenic materials for phosphorites.

Table 6
Rare earth element analysis of phosphorites in Central Guizhou, Doushantuo Formation, Ediacara (ppm).

	La	Ce	Pr	Nd	Sm	Eu	Gd	Tb	Dy	Ho	Er	Tm	Yb	Lu	Y	ΣREY	Ce/Ce*	Eu/Eu*	Ce_{anom}	Dy_N/Sm_N
BD-1	23.90	47.50	5.61	26.50	5.79	1.37	6.74	1.09	7.06	1.65	5.17	0.67	4.25	0.61	62.20	200.11	0.94	0.94	−0.07	1.55
BD-2	26.00	51.60	6.06	29.30	6.24	1.55	7.51	1.26	7.57	1.81	5.42	0.76	4.58	0.62	65.80	216.09	0.94	0.96	−0.07	1.54
BD-3	28.90	58.90	7.06	34.80	7.62	1.74	8.50	1.48	9.33	2.30	6.76	0.98	5.50	0.78	80.80	255.45	0.95	0.98	−0.07	1.56
BD-4	31.50	62.00	7.39	35.40	7.70	1.96	8.35	1.50	9.66	2.12	6.69	0.94	5.69	0.84	75.10	256.84	0.93	0.98	−0.08	1.60
BD-6	16.90	18.70	3.81	18.10	4.37	1.11	5.52	0.89	5.29	1.19	3.39	0.43	2.23	0.32	51.10	133.35	0.54	0.99	−0.32	1.54
BD-7	13.20	18.70	3.24	16.60	4.22	1.06	4.69	0.82	4.76	1.00	2.91	0.37	1.92	0.25	43.80	117.53	0.66	1.00	−0.24	1.44
BD-8	1.23	1.73	0.29	1.41	0.32	0.09	0.37	0.05	0.36	0.09	0.22	0.03	0.15	0.02	3.73	10.09	0.66	1.01	−0.23	1.44
BD-9	1.34	1.81	0.27	1.36	0.32	0.09	0.37	0.06	0.39	0.07	0.19	0.03	0.16	0.02	3.69	10.17	0.69	1.01	−0.23	1.57
BD-10	3.22	3.89	0.80	4.10	0.90	0.24	1.08	0.18	1.08	0.20	0.57	0.07	0.37	0.06	10.10	26.86	0.56	1.03	−0.31	1.54
BD-11	7.92	12.40	2.35	12.40	3.07	0.70	3.76	0.59	3.30	0.69	1.82	0.23	1.12	0.15	31.00	81.49	0.66	1.03	−0.23	1.37
BD-12	12.90	16.60	3.43	17.30	4.02	0.86	3.73	0.57	3.38	0.67	1.80	0.20	1.04	0.16	27.20	93.87	0.57	1.04	−0.29	1.07
CD-1	33.20	60.30	7.45	30.50	6.23	1.51	6.28	1.06	6.82	1.41	4.22	0.58	3.55	0.56	49.90	213.57	0.95	1.07	−0.08	1.39
CD-2	30.70	58.00	7.29	30.40	6.26	1.38	7.01	1.09	7.12	1.53	4.64	0.65	3.88	0.55	57.10	217.60	1.00	1.75	−0.08	1.45
CD-3	27.40	52.30	6.46	27.20	5.70	1.31	5.99	1.03	6.32	1.38	4.16	0.59	3.85	0.55	51.90	196.14	0.89	1.01	−0.07	1.41
CD-4	26.10	52.90	6.41	28.50	5.95	1.43	7.43	1.20	8.11	1.90	6.16	0.87	5.17	0.75	75.10	227.97	0.93	1.09	−0.06	1.73
JZ-1	41.80	93.60	14.80	79.70	26.80	6.59	31.16	4.45	22.80	4.46	12.70	1.50	8.16	1.07	158.00	507.58	0.88	1.12	−0.12	1.08
JZ-2	40.50	87.90	11.80	59.10	13.80	3.15	15.73	2.56	15.50	3.58	10.50	1.30	7.21	0.99	129.00	402.63	0.89	0.96	−0.08	1.43
JZ-3	41.20	92.10	12.50	62.00	14.00	3.35	15.53	2.62	15.80	3.58	10.30	1.37	7.78	1.01	122.00	405.15	0.90	1.04	−0.07	0.47
JZ-4	16.00	36.80	4.17	20.00	4.79	1.13	5.22	0.89	6.02	1.40	4.47	0.59	3.59	0.49	59.40	164.96	0.94	0.98	−0.03	1.44
JZ-5	9.75	22.60	2.38	11.00	2.63	0.57	2.74	0.49	3.16	0.76	2.41	0.36	1.90	0.27	33.20	94.21	0.85	1.05	−0.01	1.60
YP-1	36.60	62.30	7.63	32.30	5.71	1.70	6.23	0.94	5.53	1.25	3.69	0.44	2.75	0.37	62.00	229.45	0.92	0.99	−0.11	1.23
YP-4	5.37	6.40	1.35	7.09	1.72	0.44	2.15	0.34	1.97	0.44	1.24	0.14	0.72	0.09	20.20	49.66	1.03	1.04	−0.32	1.46
YP-5	5.69	7.60	1.75	9.58	2.20	0.55	2.51	0.44	2.59	0.56	1.57	0.19	0.97	0.12	27.00	63.33	1.08	0.98	−0.32	1.50
YP-6	15.40	19.70	3.99	18.30	4.01	0.87	3.56	0.59	3.20	0.67	1.79	0.20	1.27	0.14	25.90	99.59	0.86	1.32	−0.27	1.02
YP-7	16.70	22.30	4.63	21.70	4.97	1.04	4.82	0.72	4.35	0.85	2.31	0.28	1.42	0.17	32.40	118.66	1.00	1.06	−0.27	1.11
WQ-1	29.10	54.90	6.40	30.20	6.86	1.81	7.51	1.26	8.07	1.88	5.72	0.77	4.55	0.63	72.40	232.06	0.55	1.05	−0.08	1.50
WQ-2	10.80	19.50	2.12	9.60	2.03	0.86	2.37	0.40	2.54	0.60	2.02	0.28	1.58	0.22	27.00	81.92	0.55	1.08	−0.08	1.59
WQ-3	10.90	19.60	2.06	9.52	1.95	0.49	2.27	0.39	2.68	0.66	2.10	0.27	1.70	0.23	27.40	82.23	0.58	1.07	−0.08	1.75
WQ-4	6.09	11.80	1.19	5.83	1.15	0.48	1.37	0.24	1.55	0.39	1.29	0.20	1.09	0.17	18.20	51.04	0.58	0.99	−0.06	1.72
WQ-5	3.57	5.92	0.64	2.83	0.63	0.15	0.78	0.12	0.93	0.22	0.64	0.10	0.50	0.06	11.20	28.29	0.92	1.16	−0.10	1.88
WQ-6	24.10	44.30	5.01	22.70	5.06	1.31	6.01	1.03	7.25	1.71	5.31	0.79	4.62	0.63	70.60	200.43	0.93	1.81	−0.08	1.82
Average	18.59	35.11	4.68	22.26	5.18	1.27	5.82	0.95	5.75	1.28	3.82	0.51	2.92	0.40	49.55	158.08	0.83	1.11	−0.15	1.49
BD-5	7.56	16.20	1.88	9.09	1.94	0.46	2.23	0.39	2.48	0.58	1.88	0.26	1.51	0.22	23.80	70.48	0.99	0.99	−0.05	1.63
JZ-6	0.96	1.34	0.27	1.49	0.27	0.05	0.23	0.02	0.10	0.03	0.06	0.01	0.05	0.01	1.01	5.90	0.61	0.98	−0.28	1.53
YP-2	8.09	17.80	2.07	10.10	2.09	0.54	2.59	0.46	2.69	0.64	1.89	0.27	1.66	0.22	26.80	77.90	0.93	1.05	−0.05	1.64
YP-3	0.02	0.05	0.00	0.04	0.02	0.01	0.01	0.00	0.01	0.00	0.01	0.00	0.02	0.00	0.06	0.27	3.79	0.46	−0.07	0.48

Annotation: $Ce/Ce^* = 2Ce_{SN}/(La_{SN} + Pr_{SN})$, $Eu/Eu^* = 2Eu_{SN}/(Sm_{SN} + Gd_{SN})$ (Bau and Dulski, 1996) $Ce_{anom} = Lg(3 * Ce_N/(2 * La_N + Nd_N))$, (Haskin et al., 1968; Taylor and Mclennan, 1985). "$_{SN}$" refers to normalisation against the PAAS; "$_N$" refers to normalisation against NASC.

6.2. Redox conditions

The RSEs, including U, V, Ni, and Cr, are controlled by the redox state of the sedimentary environment and often migrate into reducing waters or sediments (Francois, 1988; Chang et al., 2009). The primary contents and compositions of RSEs can be integrally recorded because they seldom migrate after burial (Francois, 1988; Chang et al., 2009). Research has shown that V are readily enriched with sediments underlying anoxic or near-anoxic environments when compared to Ni (Calvert 1993). Therefore, a V/(V + Ni) value of > 0.46 indicates an anoxic condition, and a V/(V + Ni) value of < 0.46 indicates an oxic condition (Yarincik et al., 2000). Furthermore, 0 < V/Cr < 2.00 indicates an oxic condition, and 4.25 > V/Cr > 2.00 indicates an anoxic condition (Jones and Manning, 1994). In the V/Cr–V/(V + Ni) discriminant figures (Fig. 13a), V/Cr and V/(V + Ni) ratios record an anoxic to suboxic sedimentary condition.

U exists as insoluble U^{4+} in reducing marine environments and soluble U^{6+} in oxic marine environments. In contrast, Th appears as insoluble Th^{4+} under a supergene oxic environment, which results in oxic sediments being richer in Th than U (Kimura and Watanabe, 2001). Research has shown that Th/U ratios between 0 and 2 indicate an anoxic environment and Th/U > 3.8 indicates an oxic environment (Kimura and Watanabe, 2001). Moreover, δU is another indicator of redox environments, where δU > 1 indicates anoxic conditions and δU < 1 indicates oxic conditions (Wignall, 1991). In our study, the Th/U and δU values indicate anoxic conditions (Fig. 13b). Only a strongly reducing marine environment can cause an extremely high fractionation between U and Th. Nevertheless, V, Ni, and Cr clearly record suboxic/reducing conditions. Therefore, the redox conditions are not the only reason for the high Th–U fractionation. As discussed in Section 6.1, the rapid precipitation of U owing to hydrothermal sedimentation might be another factor responsible for these results (Rona et al., 1984).

The geochemical properties of Ce are same as those of other lanthanides in anoxic seawater. Under oxic marine environments, soluble Ce^{3+} is oxidized into insoluble Ce^{4+} as CeO_2, producing a strongly negative Ce anomaly in the modern surface oxidizing water column (Holser, 1997; Pourret et al., 2008). Therefore, Ce anomalies as redox indicators may broadly reflect changes in local oxygen availability resulting from ocean stratification (Shields and Stille, 2001). Mcarthur and Walsh (1984) suggested that negative Ce anomalies in seawater could be inherited by francolite formed under oxic seawater conditions. Generally, a Ce_{anom} value of < –0.1 shows oxic conditions and that of > –0.1 shows anoxic conditions (Haskin et al., 1968; Taylor and Mclennan, 1985). In fact, diagenetic processes may produce a negative correlation between Ce/Ce* and Dy_N/Sm_N, and a positive correlation between Ce/Ce* and total REE abundance (Morad and Felitsyn, 2001; Shields and Stille, 2001). Both correlations are nonexistent in our samples (Fig. 14g and h), suggesting that diagenetic alteration in the Ce anomaly was limited and that the Ce anomaly recorded the primary environment during the formation of phosphorite. Therefore, the Ce anomalies reflected the orignal redox condition of phosphate formation, that is, the precipitation of the precursor of the phosphatic intraclasts happened in anoxic environments. The Ce_{anom} values of phosphorites indicate a change in the marine paleoenvironment from anoxic to oxic from layer A to B. Similar observations have been made by other researchers (Chen et al., 2003; Xie et al., 2003; Wu et al., 2006).

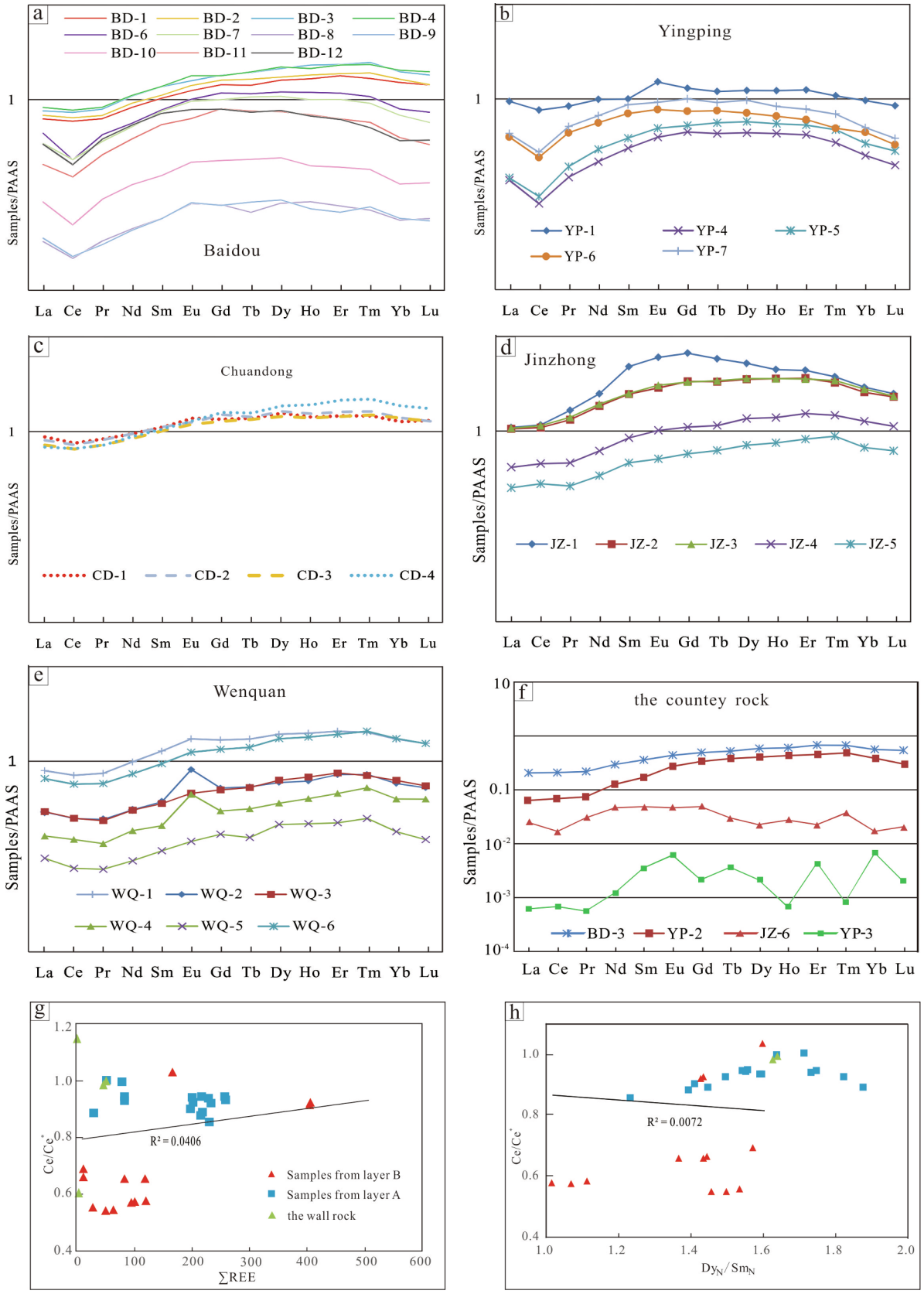

Fig. 14. a–f: The post–Archean Australian shale (PAAS)–normalized rare earth element distributions in phosphorites of Central Guizhou, Ediacaran Doushantuo Formation. The PAAS date is based on Taylor and Mclennan (1985). BD represents the Baidou ore block, CD represents the Chuangdong ore block, WQ represents the Wenquan ore block, JZ represents the Jingzhong ore block, YP represents the Yingping ore block; g: Ce/Ce*–ΣREE diagram (based on an Morad and Felitsyn (2001) and Shields and Stille (2001); h: Ce/Ce*– Dy_N/Sm_N diagram (based on Morad and Felitsyn (2001) and Shields and Stille (2001)).

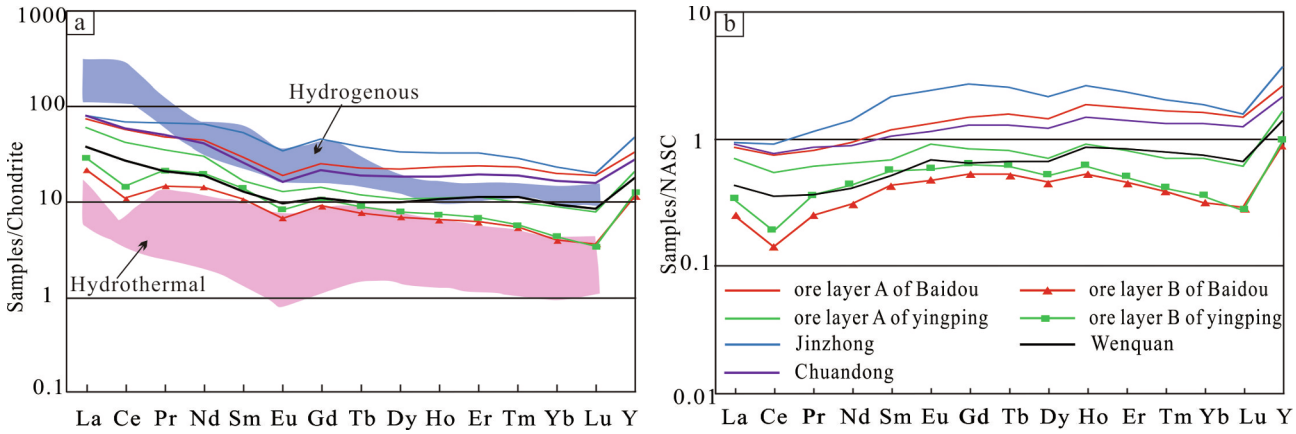

Fig. 15. Chondrite–normalized and North American shale composite (NASC) – normalized REE patterns of phosphorites from Central Guizhou, Ediacaran Doushantuo Formation. The chondrite data are from (Boynton, 1984), and the NASC date are from (Taylor and Mclennan, 1985), and the REE patterns of hydrogenous and hydrothermal deposits are from Oksuz (2011). The REE value of phosphorite and wall rocks are average.

In summary, Ni, Cr, and U were influenced by organic matter and hydrothermal processes to a certain degree, whereas the REEs were less altered. This might be the reason why the RSE indices (including V/Cr, V/(Vr + Ni), Th/U, δU), reflected inconsistent redox conditions with Ce anomalies, and the Ce anomalies were the preferable indices for recording the primary redox conditions. According to Ce_{anom} of the phosphorites, the redox condition of the Doushantuo phosphorite in Central Guizhou therefore transitioned form anoxic to oxic from layer A to B, consistent with the paleoenvironmental changes. Research has shown that the global climate became warmer, resulting in the thawing of the Marinoan Glaciers and biological "boom" after Nantuo Snowearth (Ye, 1989; Mi et al., 2010). Thereafter, in the Ediacaran Ocean, the oxygenation of seawater extended from the surface to the bottom, which resulted from the increased atmospheric oxygen content (Li et al., 2010; Fan et al., 2014; Han and Fan, 2015). The redox stratification during the Ediacaran was put forward by Jiang et al. (2007), who suggested that the seawater was stratified by oxic open-ocean shallow water and anoxic/euxinic deep water in the Yangtze Platform according to dissolved organic carbon (DOC). This has been verified by many researchers, who investigated Fe speciation, Fe isotopes, redox sensitive elements, carbon and sulfur isotopes (Goldberg et al., 2007; Canfield et al., 2008; Wille et al., 2008; Han and Fan, 2015). Along the oxygenation of seawater during the Ediacaran, the redox interface moved from shallower to deeper seawater (Li et al., 2010; Fan et al., 2014; Han and Fan, 2015). Moreover, Fan et al. (2014) studied the δ^{56}Fe of the Doushantuo Formation in the Yangtze Gorge and Wen et al. (2015) studied the $\delta^{97/95}$Mo of the Meishucun Formation in Yunnan province, and they found that the redox stratification existed both during the Doushantuo and the Meishucun periods, along with an fluctuating redox interface (Han and Fan, 2015; Liu and Zhou, 2017). This is consistent with the viewpoint that the redox stratification of Cambrian seawater inherited that of Precambrian in South China (Goldberg et al., 2007; Wille et al., 2008; Wang, 2010). Therefore, the phosphogenic event was closely related to the post-glacial global environmental change, and this may be the most direct factor responsible for the change in redox conditions from layer A to B of Doushantuo phosphorite in Central Guizhou.

According to the above discussion, the redox interface and oxygenation of seawater extended from the surface to the bottom of the Ediacaran Ocean, which was across the Yangtze Platform. However, this transition of redox conditions could not be responsible for the entire phosphogenic event across the Yangtze Platform. For example, even though formed contemporaneously with and closely to Weng'an phosphorite, Kaiyang and Zunyi phosphorites formed under anoxic conditions (Yang et al., 1997; Zhang et al., 2016), but the upper layer of Kaiyang was lacking(Wang et al., 2016). In the Hubei Doushantuo phosphorite, both the upper and lower layers of the phosphorite in Baiguoyuan, Yichang, Hushan, Three Gorges Area, and Zangcunping formed under anoxic conditions (Mi, 2010; Xin et al., 2015; Xin et al., 2016). The most important reason may be the palaeogeographic framework. Research has shown that Weng'an and Kaiyang phosphorites belong to platform-type sedimentary facies with shallower seawater, whereas cotemporaneous Zunyi, Baiguoyuan, Hushan, and Zangcunping deposits belong to basin-type sedimentary facies with deeper seawater (Yang et al., 1997) or restricted depressions (Mi, 2010; Mi et al., 2010). Along with the oxygenation extension, the shallower area was oxidized earlier than the deeper area, which is resposible for the different redox conditions of phosphogenic events across the Yangtze Platform. The Zhijin Cambrian phosphorite, located in Central Guizhou, was formed under oxic environments according to negative Ce anomalies (Shi et al., 2004; Zhang et al., 2004; Shi et al., 2006). Nevertheless, the redox condition of Meishucun phosphorite in Kunyang, Yunnan province, transformed from oxic to anoxic from the lower to the upper layer (Han and Fan, 2015; Liu and Zhou, 2017). The continuous oxygenation extension in Cambrian resulted in an oxic environment in the Meishucun period, whereas the anoxic environment recorded in the upper layer of Kunyang phosphorite might be the result of volcanic and hydrothermal activities around 535 Ma (Liu and Zhou, 2017) or secondary reworking (Mi, 2010; Wen et al., 2011).

6.3. *Apatite formation*

Layer A is mainly distributed as a grainy phosphorite with a compact banded structure, and the phosphorite mainly consist of globular phosphate intraclasts, considered to be biologically irrelevant. Layer B is distributed as dolomitic phosphorite and phosphorous dolomite, and mainly consist of microbial phosphate components and small portions of globular phosphate intraclasts. The formation of apatite is discussed in the following sections.

6.3.1. *Formation of globular phosphate intraclasts*

Most ancient phosphorites, especially Precambrian phosphorites, are characterized by high psephicity (Zhao, 1985; Ye, 1989). In our samples, the collophane have high psephicity, especially samples from layer A. In general, the granular fabric is attributed to reworking of preexisting phosphatic sediments (Ilyin, 1998; Vernhet et al., 2007; She et al., 2013; Muscente et al., 2015), involving hydrologic power capable of forcing these grains into the sediment. The sedimentary evidence for high-energy environments, such as parallel-bedding (Fig. 5a) and cross-bedding (Fig. 5c), were generally observed in these deposits and were consistent with a tidal flat environment.

The primary sedimentary textures of the Doushantuo phosphorites

are clearly reflected in the internal collophane. The microgranular sedimentary texture (Fig. 7c and d) in internal apatite is completely preserved, which resulted from the adsorption of organic matter, quartz, and other detrital components from seawater during the sedimentary process of globular phosphate intraclasts. The shrinkage cracks (Fig. 7f) resulted from the volume shrinkage of phosphate during the diagenetic process (Liu, 2008). The spongy textures (Fig. 7g and h) resulted from phosphatization during the diagenetic process (Liu, 2008). The isopachous cement (Fig. 7e and f) is also considered a diagenetic texture, consistent with cement as viewed under an optical microscope (Xie et al., 2003; She et al., 2013). Liu and Chen (1994) suggested that the bright cement formed in the pore water in sediments during diagenesis, regarded as first-generation cement by other researchers (Zhao, 1985; She et al., 2013). The second-generation cement is dolomite rather than quartz as reported previously (Zhao, 1985; She et al., 2013). The primary sedimentary fabrics of globular collophane demonstrate that the phosphorite formed under strong mechanical power and underwent reworking of pre-existing phosphatic sediments. Therefore, we suggest that the Doushantuo granular phosphorites in layer A were formed by the reworking of previous phosphatic sediments, consistent with previous research (Follmi, 1996), and the mechanical power of seawater played an important role in forming the granular collophane. The intact crystallographic form of crystallites (Fig. 7k–o) suggested that alteration after diagenesis was limited.

Though the texture of the collophane indicates the reworking of pre-existing phosphatic sediments, the process in which P and other elements transformed into phosphatic sediments remains in question. Previous studies have shown that phosphate is under-saturated even in P-rich normal marine environments (Yang et al., 1997), and thus phosphate is less likely to directly precipitate from seawater. Pufahl and Grimm (2003) suggested that in situ diagenetic mineralization driven by changes in pore water redox potential could have been responsible for the phosphogenic event, which is also called the “Fe-redox” pump. The model suggested that the soluble phosphate group PO_4^{3-} was introduced by iron hydroxides (FeOOH) as a kind of adsorptive complex compound (Shaffer, 1986; Muscente et al., 2015). When $FeOOH{\cdot}PO_4^{3-}$ ionic group dropped from the redox interface, Fe^{3+} was reduced to Fe^{2+} in the water column, and PO_4^{3-} was released into the sediments (Cappellen and Berner, 1988; Shen et al., 2000; Jiang et al., 2011; Pufahl and Hiatt, 2012). The total Fe content of the phosphorite samples ranked from 0.05 to 2.63%, with an average of 0.86%, confirming the possibility of Fe participating in mineralization. Redox stratification was prevalent in the Ediacaran and Cambrian oceans (Mazumdar et al., 1999; Goldberg et al., 2007; Fan et al., 2014; Han and Fan, 2015). Ce anomalies and RSE indices indicated that phosphogenesis occurred beneath the redox interface, which is consistent with the redox stratification of seawater and beneficial to the “Fe-redox” pump.

Thus, we propose a globular apatite formation process, which is divided into the following five formation stages: (1) P-bearing sediment precipitation, during which soluble P was carried to the redox interface as the $FeOOH{\cdot}PO_4^{3-}$ ionic group, and then PO_4^{3-} was released into the sediments. (2) Phosphatization stage, during which the released PO_4^{3-} combined with F^-, Ca^{2+}, and other metallogenic elements and then transformed into phosphate through phosphatization. At the same time, the spongy textures and shrinkage cracks formed becausde of the formation of microcrystalline apatite and volume shrinkage. (3) Mechanical disruption of phosphate, during which incompletely consolidated phosphate was disrupted and irregular phosphate particles formed through mechanical hydrodynamic forces, such as tide activities and waves. (4) The rounded and re-precipitated stage, involved disrupted and irregular particles being carried in the turbulent seawater and re-precipitated. Importantly, in this process, irregular particles were elutriated and rounded, resulting in the high psephicity of the apatite. (5) The growth of isopachous apatite cement involved well-ordered apatite cement being formed in the pore water of the sediments, forming the first-generation cement. In the diagenetic stages, apatite granules were cemented by dolomite which serves as the second-generation cement.

6.3.2. Formation of microbial phosphate component

Organic matter has been proposed as a possible primary REE carrier (Reynard et al., 1999), and REE fractionation occurs during such transport. Researchers have shown that the biogenic apatite are rich in MREEs (Mcarthur and Walsh, 1984; Kidder and Eddy-Dilek, 1994; Felitsyn and Morad, 2002), because they are substituted for Ca^{2+} in the apatite lattice when biogenic apatite is formed (Wright et al., 1990). In our samples, the PAAS–normalized REE distributions of layer B are characterized by a “hat-shaped” REE plot (Fig. 14a and b), indicating that microorganisms or organic matter participated in the mineralization process. Research has shown that As, Sr, and Ba can be adsorbed by microorganisms, and that the microorganisms can react with Pb and Cu to produce metal complex compounds (Gulbrandsen, 1969). These trace elements were rich in Weng’an and Kaiyang phosphorites to a certain degree, indicating that microorganisms were likely involved in mineralization. As, Pb, and Sr are also related to hydrothermal sedimentation, but no evidence has been provided to certify the amount of trace element that microorganisms or hydrothermal processes each could have contributed.

Previous studies on Doushantuo phosphorite mainly focused on the classification and three-dimensional feature of the microfossils, which were interpreted as algae (Xue et al., 1995; Xiao et al., 1998; Mi et al., 2010; Igisu et al., 2014), animal embryos (Xiao et al., 1998; Yin et al., 2007a, 2007b; Igisu et al., 2014), acritarchs (Zhou et al., 2007; Muscente et al., 2015), and non-metazoan holozoans (Therese et al., 2012). In this study, the role of microorganisms in P enrichment was discussed in detail, and the microfossils were differentiated as embryo- and algae-like microfossils rather than classifying them in detail.

All the phosphatic microfossils and biogenic apatite indicated that the formation of the microbial phosphate component was dominated by microorganisms. Generally, microorganisms take part in P enrichment by adsorbing metallogenic elements directly (Liang et al., 1984; She et al., 2013) or changing the metallogenic conditions. The primary growing texture of embryo-like microfossils and the inner texture (Fig. 8a–e) of algae-like microfossils (Fig. 8f–j) indicated that microorganisms adsorbed P and other elements during growth. The cleavage stages of the embryos represent their successive binary divisions (Yin et al., 2007a, 2007b). The characteristics of the simple to aggregated algae indicated that the apatite might have grown by surrounding the algae (dark–gray contrast). The aggregated entities (Fig. 8i, k, and l) were formed by multiple incipient individuals, indicating that spheroid algae were cemented by apatite soon after death. Linear principal component analyses of the irregularly concentric apatite indicate that Ca, P, O, and F are characterized by periodic changes along with the periodic changes in contrast observed in BSE images, and the lowest contents are recorded by the algae in the center of apatite (Fig. 10). She et al. (2013) analyzed the micro-textures of Doushantuo globular apatite (Yichang, Hunan) by SEM, Raman spectroscopy, and NanoSIMS and suggested that excess extracellular polymeric substances (EPS) produced by microorganisms were expected to adsorb the elements and control the precipitation of biological apatite. This viewpoint is consistent with the suggestion of other researchers in that EPS served as a primary substrate and defined the laminated character of the granules (Heike and Wolfgang, 2000; Liu et al., 2004; Lopez et al., 2011). This is also in accord with the microbial phosphorite component, especially the pistil-like apatite (Fig. 10g), irregularly concentric apatite (Fig. 10h), and concentrically zoned granules (Fig. 10p). Therefore, we suggest that the growth of microorganisms might relate to the periodic changes of P in seawater resulting from the adsorption of metallogenic materials by microorganisms during apatite precipitation.

There are also differences between the studies of She et al. (2013) and the results of this study. The phosphatized microfossils of Yichang formed under anoxic environments (Mi et al., 2010; Xin et al., 2015; Xin

et al., 2016), and the microfossils were well preserved after precipitation. Whereas Weng'an microbial phosphorite formed under oxic environments, partial algal microorganisms were oxidized and degraded before buried and P being released into pore water (Longinelli and Nuti, 1973; Shen et al., 2000). The damaged algal microfossils (Fig. 10q) indicated that partial algal microorganisms were degraded before they were burried completely. This led to high P content of the pore water, and then the amorphous apatite (Fig. 10r) formed during diagenesis. This kind of amorphous apatite mutually cemented with dolomite (Fig. 10r), indicating that they formed simultaneously and served as second-generation cement. The differences between Weng'an and Yichang microbial phosphorite might be due to the redox conditions that influenced the conservation of microorganisms.

The Doushantuo microbial phosphorites shed light on the shallow marine environment after the Marinoan glaciation. Both geochemical characteristics and micro-textures of biogenic apatite (Fig. 8) suggest a genetic link between microorganisms and apatite. We suggest a microbial phosphate forming process divided into the following four formation stages: (1) Under oxic and nutrition-rich conditions, microorganisms adsorbed P for the demands of growth, forming the incipient algal tissues (Fig. 8f–j). The algae produced EPS, which provided nucleation sites and adsorbed P, Ca, F, pyrite, quartz, and other detrital components (Liang et al., 1984; She et al., 2013). (2) P in seawater was adsorbed by EPS, and oxygen was consumed, which resulted in decreased P content and anoxic conditions in local regions. Thereafter, P and O were supplied from the surrounding seawater, producing periodic changes in P in local seawater and forming the irregularly concentric textures (Fig. 8f–h), which resulted in periodic changes in P contents during accretionary growth (Fig. 10). (3) During the intermittent P-depleted and microorganism-free stages, microorganisms died and precipitated in sediments, and F-bearing calcium phosphate was subsequently formed through phosphatization. Partial algal microorganisms were degraded before being buried completely, causing P to be released into pore water. (4) The isopachous cement was formed in pore water without microbial action and served as first-generation cement. This stage was similar to the last formation stage of the globular apatite. Thereafter, the amorphous apatite formed because the excess P released by degraded algal during the diagenetic stages. And then the amorphous apatite was mutually cemented with dolomite, serving as the second-generation cement.

The geochemical data showed that the redox conditions transitioned from anoxic to oxic from layer A to B. Therefore, we considered the possibility that redox conditions influenced the transition of genetic mechanisms. In the earlier depositional stages of the Doushantuo phosphorites, the sedimentary environment remained anoxic at the sediment–water interface after the Marinoan glacier melted. Many transgressions occurred, and the hydrothermal fluids and normal seawater invaded the shallow water environment. The globular phosphate intraclasts formed through the reworking of pre-existing phosphatic sediment. In the later depositional stages of the Doushantuo Formation, the sedimentary environment became oxic with the increased oxygenation of the seawater. Microorganisms flourished and played a dominant role in the formation of biogenic apatite. It can be concluded that the phosphogenic events occurred near the redox interface in the seawater surrounding the Doushantuo Formation, and the dominant metallogenic mechanism of the phosphorite in layer A was the mechanical power of the seawater, whereas the driving mechanism of metallogenesis in layer B phosphorite was microorganisms.

7. Conclusions

The following conclusions can be drawn from the apatite microtextures, in situ major elements of apatite and the geochemical characteristics of the phosphorites:

1. Phosphogenesis occurred during the deposition of the Doushantuo Formation and was restricted to tidal flats, which resulted from marine transgressions. Geochemical analyses suggest that hydrothermal processes might have contributed to the metallogenic materials in these strata. Hydrothermal fluids would have been injected into the bottom of the water column, mixing with normal seawater. This mixture of hydrothermal fluids and normal seawater would have invaded the shallow water basins, providing metallogenic materials.

2. The phosphogenic events occurred under anoxic conditions for layer A and oxic conditions for layer B. This was consistent with the viewpoint that the redox interface extended from the surface to the bottom in the Ediacaran Ocean. However, this transition of redox conditions could not be responsible for the entire phosphogenic event across the Yangtze Platform.

3. We suggest that the globular intraclasts from layer A were formed by the reworking of previous phosphoric sediments, which were influenced by the strong mechanical power of seawater. A globular apatite formation process was proposed, which could be divided into five stages: P-bearing sediment precipitation, phosphatization stage, mechanical disruption of phosphate, the rounded and re-precipitated stage, and growth of isopachous apatite cement. The microbial phosphate component of layer B was formed by microbially mediated accretionary growth. Phosphatization occured in most microorganisms, while partial algal microorganisms were degraded before being buried entirely, resulting to that algal microfossils were damaged and P released into the pore water. The amorphous apatite formed during the diagenetic stages and mutually cemented with dolomite, serving as second-generation cement.

4. The transition of redox conditions might be responsible for the genetic mechanism transition of phosphate particles. Whereas, the P content in ore minerals of different phosphorites had no connection to their genetic mechanisms. However, there may be other factors worth considering to reveal why there was a lower P_2O_5 content in layer B than in layer A in Doushantuo phosphorites, Central Guizhou.

Declaration of Competing Interest

This manuscript has not been published or presented elsewhere in part or in entirety, and it is not under consideration by another journal. All the authors have approved the manuscript and agree with submission to your esteemed journal. There are no conflicts of interest to declare.

Acknowledgments

The authors are grateful to Dr. Chengquan Wu and Dr. Jianbing Duan for their helpful suggestions toward improving the quality of this manuscript. This work was supported through the Public Beneficial, Basic Geological Project of Depatment of Land and Resources of Guizhou Province (2016-09-1), the 12th Five Year Plan Project of the State Key Laboratory of Ore Deposit Geochemistry at the Chinese Academy of Science (SKLODG-Zy125-08) and the National Basic Research Program of China (2014CB440906).

Appendix A. Supplementary material

Supplementary data to this article can be found online at https://doi.org/10.1016/j.jseaes.2019.103931.

References

Baar, H.J.W.D., Bacon, M.P., Brewer, P.G., Bruland, K.W., 1985. Rare earth elements in the Pacific and Atlantic Oceans. Geochim. Cosmochim. Acta 49 (9), 1943–1959.
Baturin, G.N., 1981. Phosphorites on the Sea Floor. Elservier Scient ific Publish ing Company, New York.
Bau, M., Dulski, P., 1996. Distribution of yttrium and rare-earth elements in the Penge and Kuruman iron-formations, Transvaal Supergroup, South Africa. Precambrian Res. 79 (1–2), 37–55.
Bau, M., Möller, P., 1992. Rare earth element fractionation in metamorphogenic

hydrothermal calcite, magnesite and siderite. Mineral. Petrol. 45, 231–246.
Benmore, R.A., 1983. Origin of sedimentary francolite forms its surfur and carbon isotope composition. Nature 302, 516–518.
Boström, K., 1983. Genesis of Ferromanganese Deposits-Diagnostic Criteria for Recent and Old Deposits. Springer, US.
Boynton, W.V., 1984. Cosmochemistry of the rare earth elements: meteorite studies. Develop. Geochem. 2 (2), 63–114.
Calvert, S.E.P.T.F., 1993. Geochemistry of Recent oxic and anoxic marine sediments: implications for the geological record. Mar. Geol. 113 (1–2), 67–88.
Canfield, D.E., Poulton, S.W., Knoll, A.H., Narbonne, G.M., Ross, G., Goldberg, T., Strauss, H., 2008. Ferruginous conditions dominated later neoproterozoic deep-water chemistry. Science 321 (5891), 949–952.
Cappellen, P.V., Berner, R.A., 1988. A mathematical model for the early diagenesis of phosphorus and fluorine in marine sediments; apatite precipitation. Am. J. Ofence 288 (4), 289–333.
Chang, H.J., Chu, X.L., Feng, L.J., 2009. Redox sensitive trace elements as paleoenvironments proxies. Geol. Rev. 55 (1), 91–99.
Chen, D.F., Dong, W.Q., Qi, L., Chen, G.Q., Chen, X.P., 2003. Possible REE constraints on the depositional and diagenetic environment of Doushantuo Formation phosphorites containing the earliest metazoan fauna. Chem. Geol. 201 (1–2), 103–118.
Chen, G.Y., Du, Y.S., Zhang, Y.G., Chen, Q.G., Fan, Y.M., Wang, Z.P., Tan, H., 2015. Spatial and temporal variation and mineralization model of the sinian phosphorus-bearing sequences in Central Guizhou Province. Geol. Sci. Technol. Inform. 34, 18–25 (in Chinese with English abstract).
Chu, X.L., Feng, L.Y., Chen, Q.Y., 1995. Sulfur isotope and its significance of the Late Sinian phosphorites in Kaiyang District, Guizhou Province. Chinese Sci. Bull. 40 (3) 239 239 (in Chinese with English abstract).
Deng, K.Y., Bo, W.U., Luo, M.X., Luo, C., Long, J.X., 2015. Phosphate rock geochemistry of the doushantuo formation in shuangshanping, Kaiyang of Guizhou Province and its genetic significance. Geol. Explor. 51, 123–132 (in Chinese with English abstract).
Dong Ye, M., 1996. Uppwellin goceanic curuents & Epicontinental Chi. Geol. Chem. Miner. 18, 156–162 (in Chinese with English abstract).
Dong Ye, M., 2001. Regional ore-forming regulation of phosphorite in Yangtze massif in the times of Doushantuo and Meishucun ages. Geol. Chem. Miner. 23, 193–209 (in Chinese with English abstract).
Douville, E., Bienvenu, P., Charlou, J.L., Donval, J.P., Fouquet, Y., Appriou, P., Gamo, T., 1999. Yttrium and rare earth elements in fluids from various deep-sea hydrothermal systems. Geochim. Cosmochim. Acta 63 (5), 627–643.
Fan, H.F., Zhu, X.K., Wen, H.J., Yan, B., Li, J., Feng, L.J., 2014. Oxygenation of Ediacaran Ocean recorded by iron isotopes. Geochim. Cosmochim. Acta 140, 80–94.
Felitsyn, S., Morad, S., 2002. REE patterns in latest Neoproterozoic-early Cambrian phosphate concretions and associated organic matter. Chem. Geol. 187 (3), 257–265.
Follmi, K.B., 1996. The phosphorus cycle, phosphogenesis and marine phosphate-rich deposits. Earth Sci. Rev. 40 (1–2), 55–124.
Föllmi, K.B., 1996. The phosphorus cycle, phosphogenesis and marine phosphate-rich deposits. Earth Sci. Rev. 40 (1–2), 55–124.
Francois, R., 1988. A study on the regulation of the concentrations of some trace metals (Rb, Sr, Zn, Pb, Cu, V, Cr, Ni, Mn and Mo) in Saanich Inlet Sediments, British Columbia,Canada. Mar. Geol. 83 (1), 285–308.
Frohlich, P.N., Kim, K.H., Jahnke, R., Burnett, W.C., Soutar, A., Deakin, M., 1983. Pore water fluoride in Peru continental margin sediments: uptake from seawater. Geochim. Cosmochim. Acta 47 (9), 1605–1612.
Goldberg, E.D., Koide, M., Schmitt, R.A., Smith, R.H., 1963. Rare-Earth distributions in the marine environment. J. Geophys. Res. 68 (14), 4209–4217.
Goldberg, T., Strauss, H., Guo, Q., Liu, C., 2007. Reconstructing marine redox conditions for the early Cambrian Yangtze Platform: evidence from biogenic sulphur and organic carbon isotopes. Palaeogeogr. Palaeoclimatol. Palaeoecol. 254 (2), 175–193.
Gulbrandsen, R.A., 1969. Physical and chemical factors in the formation of marine apatite. Econ. Geol. 67 (6), 824–827.
Guo, Q.J., Yang, W.D., Liu, C.Q., Strauss, H., Wang, X.L., 2003. Sedimentary geochemistry research on the radiation of Weng'an biota and the formation of the phosphorite ore deposit, Guizhou. Bull. Mineral. Petrol. Geochem. 22, 11–17 (in Chinese with English abstract).
Han, T., Fan, H.F., 2015. Dynamic evolution of the Ediacaran ocean across the Doushantuo Formation, South China. Chem. Geol. 417, 261–272.
Harrison, A., Thode, H., 1958. Mechanism of the bacterial reduction of sulphate from isotope fractionation studies. Trans. Faraday Soc. 54, 84–92.
Haskin, L.A., Wildeman, T.R., Haskin, M.A., 1968. An accurate procedure for the determination of the rare earths by neutron activation. J. Radioanalyt. Chem. 1 (4), 337–348.
He, X.Q., Xiao, J.F., Wang, S.Y., Liu, A.M., Chao, L.I., Ping, B., 2005. The study on the Qianzhong upheaval. Guizhou Geol. 22, 5–21 (in Chinese with English abstract).
Heike, V.K., Wolfgang, E.K., 2000. Bacterial calcification. Microbial Sediments 25–31.
Henderson, P., 1984. Rare Earth Element Geochemistry. Geological Publishing House.
Holser, W.T., 1997. Evaluation of the application of rare-earth elements to paleoceanography. Palaeogeogr. Palaeoclimatol. Palaeoecol. 132 (1–4), 309–323.
Igisu, M., Komiya, T., Kawashima, M., Nakashima, S., Ueno, Y., Han, J., Shu, D., Li, Y., Guo, J., Maruyama, S., 2014. FTIR microspectroscopy of Ediacaran phosphatized microfossils from the Doushantuo Formation, Weng'an, South China. Gondwana Res. 25 (3), 1120–1138.
Ilyin, A.V., 1998. Rare-earth geochemistry of 'old' phosphorites and probability of syngenetic precipitation and accumulation of phosphate 1 In memory of Richard P. Sheldon 1. Chem. Geol. 144 (3), 243–256.
Jiang, G.Q., Kaufman, A.J., Christie-Blick, N., Zhang, S.H., Wu, H.C., 2007. Carbon isotope variability across the Ediacaran Yangtze platform in South China: implications for a large surface-to-deep ocean δ 13 C gradient. Earth Planet. Sci. Lett. 261 (1–2), 303–320.
Jiang, G.Q., Shi, X.Y., Zhang, S.H., Wang, Y., Xiao, S.H., 2011. Stratigraphy and paleogeography of the Ediacaran Doushantuo Formation (ca. 635–551 Ma) in South China. Gondwana Res. 19 (4), 831–849.
Jiang, G.Q., Sohl, L.E., Christieblick, N., 2003. Neoproterozoic stratigraphic comparison of the Lesser Himalaya (India) and Yangtze block (south China): paleogeographic implications. Geology 31 (10), 917–920.
Jones, B., Manning, D.A.C., 1994. Comparison of geochemical indices used for the interpretation of palaeoredox conditions in ancient mudstones. Chem. Geol. 111 (111), 111–129.
Kidder, D.L., Eddy-Dilek, C.A., 1994. Rare-earth element variation in phosphate nodules from midcontinent Pennsylvanian cyclothems. J. Sed. Res. - Section A; (United States) 64: 3(3), 584–592.
Kimura, H., Watanabe, Y., 2001. Oceanic anoxia at the Precambrian-Cambrian boundary. Geology 29 (11), 995.
Li, C., Love, G.D., Lyons, T.W., Fike, D.A., Sessions, A.L., Chu, X., 2010. A stratified redox model for the Ediacaran ocean. Science 328 (5974), 80–83.
Liang, T.Y., Chang, A.Z., Zhang, M.T., Chen, Y.C., 1984. Of the research of texture, characteristics and genetic mechanism of francolite. J. Jiling Univ. 14, 35–43 (in Chinese with English abstract).
Liu, B.J., 1987. Storm events and phosphate deposition in Cambrian on the western margin of the Yangtze platform, China. Acta Sedimentol. Sin. 5, 28–39 (in Chinese with English abstract).
Liu, B.J., Xu, X.S., Xu, Q., Pan, X.N., Huang, H.Q., 1993. Sedimentary Crustal Evolution and Mineralization of Palaeocontinent in South China. Scientific Publications, Beijing.
Liu, K.W., Chen, Q.Y., 1994. Cementation processes of phosphorites. Scientia Geologica Sinica 29 (1), 62–70.
Liu, S.R., 2008. Study of the mineralization process of zhijin xinhua phosphate deposit using microbeam analyses. academic dissertation, institute of geochemistry. Chinese Acad. Sci (in Chinese).
Liu, Y.J., Cao, L.M., 1987. Int roduction of Elemental Geochem istry Geoloygal Press (in Chinese), Beijing.
Liu, Y.Q., Liu, Y., Tay, J.H., 2004. The effects of extracellular polymeric substances on the formation and stability of biogranules. Appl. Microbiol. Biotechnol. 65 (2), 143–148.
Liu, Z.R., Zhou, M.F., 2017. Meishucun phosphorite succession (SW China) records redox changes of the early Cambrian ocean. Geol. Soc. Am. Bull. (11–12), 1554–1567.
Longinelli, A., Nuti, S., 1973. Revised phosphate-water isotopic temperature scale. Earth Planet. Sci.Lett. 3, 373–376.
Lopez, C.J., Chekroun, K.B., Jroundi, F., Gallego, M.R., Arias, J.M., González-Muñoz, M.T., 2011. Myxococcus xanthus Colony Calcification: an study to better understand the processes involved in the formation of this stromatolite-like structure. Adv. Stromatolite Geobiol. 131, 161–181.
Marchig, V., Gundlach, H., Möller, P., Schley, F., 1982. Some geochemical indicators for discrimination between diagenetic and hydrothermal metalliferous sediments. Mar. Geol. 50 (3), 241–256.
Mazumdar, A., Banerjee, D.M., Schidlowski, M., Balaram, V., 1999. Rare-earth elements and stable isotope geochemistry of early Cambrian chert-phosphorite assemblages from the Lower Tal formation of the Krol Belt (Lesser Himalaya, India). Chem. Geol. 156 (1–4), 275–297.
Mcarthur, J.M., Walsh, J.N., 1984. Rare-earth geochemistry of phosphorites. Chem. Geol. 47 (3), 191–220.
Mi, W.T., 2010. The sequence stratigraphy and genesis of phosphorites of doushantuo formation at Baiguoyuan, Yichang, Hubei. Acta Sedimentologica Sinica 28 (3), 471–480.
Mi, W.T., Lin, L., Ma, Y.Q., Wang, X.L., Ren, C.Y., Zhou, Y.H., 2010. Sedimentary sequence of phosphatic rock series and formation of phosphorites in the Doushantuo formation in weng'an, Guizhou. Sed. Geol. Tethyan Geol. 9 (30), 46–52 (in Chinese with English abstract).
Morad, S., Felitsyn, S., 2001. Identification of primary Ce-anomaly signatures in fossil biogenic apatite: implication for the Cambrian oceanic anoxia and phosphogenesis. Sed. Geol. 143 (3–4), 259–264.
Muscente, A.D., Hawkins, A.D., Xiao, S., 2015. Fossil preservation through phosphatization and silicification in the Ediacaran Doushantuo Formation (South China): a comparative synthesis. Palaeogeogr. Palaeoclimatol. Palaeoecol. 434 (4331), 46–62.
Nathan, Y., Nielsen, H., 1980. Sulfur isotope in phosphorites. SEPM Special Publication No. 29 73–78.
Oksuz, N., 2011. Geochemical characteristics of the Eymir (Sorgun-Yozgat) manganese deposit, Turkey. J. Rare Earths 29 (3), 287–296.
Olivarez, A.M., Owen, R.M., 1991. The europium anomaly of seawater: implications for fluvial versus hydrothermal REE inputs to the oceans. Chem. Geol. 92 (4), 317–328.
Pourret, O., Davranche, M., Gruau, G., Dia, A., 2008. New insights into cerium anomalies in organic-rich alkaline waters. Chem. Geol. 251 (1–4), 120–127.
Pufahl, P.K., Grimm, K.A., 2003. Coated phosphate grains: Proxy for physical, chemical, and ecological changes in seawater. Geology 31 (9), 801–804.
Pufahl, P.K., Hiatt, E.E., 2012. Oxygenation of the Earth's atmosphere-ocean system: a review of physical and chemical sedimentologic responses. Mar. Pet. Geol. 32 (1), 1–20.
Qi, L., Hu, J., Gregoire, D.C., 2000. Determination of trace elements in granites by inductively coupled plasma mass spectrometry. Talanta 51 (3), 507.
Reynard, B., Lécuyer, C., Grandjean, P., 1999. Crystal-chemical controls on rare-earth element concentrations in fossil biogenic apatites and implications for paleoenvironmental reconstructions. Chem. Geol. 155 (3–4), 233–241.
Rona, P.A., Boström, K., Laubier, L., Jr, K.L.S., 1984. Processes in the Ocean. (Book Reviews: Hydrothermal Processes at Seafloor Spreading Centers). Science 226(4678).
Shaffer, G., 1986. Phosphate pumps and shuttles in the Black Sea. Nature 321 (6069),

515–517.
She, Z.B., Strother, P., Mcmahon, G., Nittler, L.R., Wang, J.H., Zhang, J.H., Sang, L.K., Ma, C.Q., Papineau, D., 2013. Terminal Proterozoic cyanobacterial blooms and phosphogenesis documented by the Doushantuo granular phosphorites I: In situ microanalysis of textures and composition. Precambr. Res. 235 (3), 20–35.
She, Z.B., Strother, P., Papineau, D., 2014. Terminal Proterozoic cyanobacterial blooms and phosphogenesis documented by the Doushantuo granular phosphorites II: Microbial diversity and C isotopes. Precambr. Res. 251 (3), 62–79.
Shen, Y., Schidlowski, M., Chu, X.L., 2000. Biogeochemical approach to understanding phosphogenic events of the terminal Proterozoic to Cambrian. Palaeogeogr. Palaeoclimatol. Palaeoecol. 158 (1), 99–108.
Shi, C.H., 2005. Formation of phosphorite deposit, Breakup of Rodinia supercontinent and Biology explosion – a case study of Weng'an, Kaiyang and Zhijin phosphorite deposits of Guizhou Province. Academic dissertation, The Key Laboratory of Ore Deposit Geochemistry, Institute of Geochemistry. Chinese Acad. Sci (in Chinese).
Shi, C.H., Hu, R.Z., Wang, G.Z., 2004. Study on REE geochemistry of Zhijin phosphorites, Guizhou province. J. Min. Petrol. 22 (4), 71–75.
Shi, C.H., Hu, R.Z., Wang, G.Z., 2006. Element geochemistry of Zhijin phosphorites, Guizhou province. Acta Mineralogica Sinica 26 (2), 169–174.
Shields, G., Stille, P., 2001. Diagenetic constraints on the use of cerium anomalies as palaeoseawater redox proxies: an isotopic and REE study of Cambrian phosphorites. Chem. Geol. 175 (1–2), 29–48.
Shu, L.S., 2012. An analysis of principal features of tectonic evolution in South China Block. Geol. Bull. China 31 (7), 1035–1053.
Strauss, H., 1999. Geological evolution from isotope proxy signals - sulfur. Chem. Geol. 161 (1), 89–101.
Sverjensky, D.A., 1984. Europium redox equilibria in aqueous solution. Earth Planet. Sci. Lett. 67 (1), 70–78.
Taylor, S.R., Mclennan, S.M., 1985. The Continental Crust: Its Composition and Evolution, An Examination of the Geochemical Record Preserved in Sedimentary Rocks. Scientific Publications, Blackwell, pp. 1–312.
Therese, H., Cunningham, J.A., Chongyu, Y., Marco, S., Federica, M., Donoghue, P.C.J., Stefan, B., 2012. Fossilized nuclei and germination structures identify Ediacaran "animal embryos" as encysting protists. Science 335 (6073), 1696–1699.
Van Waveren, I.M., Marcus, N.H., 1993. Morphology of recent copepod egg envelopes from Turkey Point, Gulf of Mexico, and their implications for acritarch affinity. Spec. Pap. Palaeontol. 48, 111–124.
Vernhet, E., Heubeck, C., Zhu, M.Y., Zhang, J.M., 2007. Stratigraphic reconstruction of the Ediacaran Yangtze Platform margin (Hunan Province, China) using a large olistolith. Palaeogeogr. Palaeoclimatol. Palaeoecol. 254 (1–2), 123–139.
Wang, J., Li, Z.X., 2003. History of Neoproterozoic rift basins in South China: implications for Rodinia break-up. Precambr. Res. 122 (1), 141–158 (in Chinese with English abstract).
Wang, J., Zeng, Z.G., Chen, W.X., Wang, Z.J., Xiong, G.Q., Wang, X.H., 2006. The Neoproterozoic rift systems in southern China: New evidence for the sedimentary onlap and its initial age. Sed. Geol. Tethyan Geol. 26 (4), 1–7 (in Chinese with English abstract).
Wang, X.Q., 2010. Organic carbon isotope evidence for late Ediacaran - early Cambrian ocean stratification in South China. China University of Geosciences (Beijing).
Wang, Y.G., Zhu, S.X., 1984. New progress in the study of phosphorus strata and phosphorite of Doushantuo Formation, the Central Guizhou. Reginal geology of China. Geol. Bull. China 1 135 135 (in Chinese with English abstract).
Wang, Z.G., Ding, X.Y., Zhao, Z.H., 1989. Rare Earth Element Geochemistry. Scientific Publications, Beijing.
Wang, Z.P., Zhang, Y.G., Du, Y.S., Chen, G.Y., Liu, J.Z., Xu, Y.Y., Tan, D.W., Li, L., Wang, D.F., Wu, W.M., 2016. Reconstruction of quantitative lithofacies palaeogeography of the Sinian Doushantuo Age of phosphorite depositional zone in Kaiyang area, central Guizhou Province. J. Palaeogeogr. 18 (3), 399–410 (in Chinese with English abstract).
Wen, H., Carignan, J., Zhang, Y., Fan, H., Cloquet, C., Liu, S., 2011. Molybdenum isotopic records across the Precambrian-Cambrian boundary. Geology 39 (8), 775–778.
Wen, H., Fan, H., Zhang, Y., Cloquet, C., Carignan, J., 2015. Reconstruction of early Cambrian ocean chemistry from Mo isotopes. Geochim. Cosmochim. Acta 164, 1–16.
Wignall, P.B., 1991. Model for transgressive black shales? Geology 19 (2), 167.
Wille, M., Nagler, T.F., Lehmann, B., Schroder, S., Kramers, J.D., 2008. Hydrogen sulphide release to surface waters at the Precambrian/Cambrian boundary. Nature 453 (7196), 767–769.
Wright, J., Schrader, H., Holser, W.T., 1990. Paleoredox variations in ancient oceans recorded by rare earth elements in fossil apatite. Geochim. Cosmochim. Acta 51 (3), 631–644.
Wu, C.Z., Xiong, R.L., Xiang, L.E., 1984. The paleogeographic characteristics and mineralization of the early Sinian phosphorite, in Northwest Hunan. Proceedings of the Fifth International Symposium of Phosphorite. Geological Publishing House, Beijing.
Wu, K., Ma, D.S., Pan, J.Y., Nie, W.M., Zhou, J., Xia, F., Liu, L., 2006. The geochemistry of phosphorite of Doushantuo Formation in Weng'an, China: insights from trace elements and REE. J. East China Inst. Technol. 29, 108–114 (in Chinese with English abstract).
Xiao, S.H., Knoll, A.H., 2000. Phosphatized animal embryos from the Neoproterozoic Doushantuo Formation at Weng'An, Guizhou, South China. J. Paleontol. 74 (5), 767–788.
Xiao, S.H., Zhang, Y., Knoll, A.H., 1998. Three-dimensional preservation of algae and animal embryos in a Neoproterozoic phosphorite. Nature 391 (6667), 553–558.
Xie, Q.L., Chen, D.F., Qi, L., Chen, X.P., 2003. Ree geochemistry of doushantuo phosphorites and paleoenvironmental changes in weng'an area, south China. Acta Mineralogica Sinica 23 (4), 289–295 (in Chinese with English abstract).
Xin, H., Jiang, S., Yang, J., Wu, H., Pi, D., 2016. Rare Earth Element Geochemistry of Phosphatic Rocks in Neoproterozoic Ediacaran Doushantuo Formation in Hushan Section from the Yangtze Gorges Area, South China. J. Earth Sci. 27 (2), 204–210.
Xin, H., Jiang, S.Y., Yang, J.H., Wu, H.P., Pi, D.H., 2015. Rare earth element and Sr-Nd isotope geochemistry of phosphatic rocks in Neoproterozoic Ediacaran Doushantuo Formation in Zhangcunping section from western Hubei Province, South China. Palaeogeogr. Palaeoclimatol. Palaeoecol. 440, 712–724.
Xue, Y.S., Tang, T.F., Yu, C.L., Zhou, C.M., 1995. Large spheroidal Chlorophyta fossils from the Doushantuo Formation phosphoric sequence (late Sinian), Central Guizhou, South China. Acta Palaeontologica Sinica 34, 688–706 (in Chinese with English abstract).
Yamamoto, K., 1987. Geochemical characteristics and depositional environments of cherts and associated rocks in the Franciscan and Shimanto Terranes. Sed. Geol. 52 (1), 65–108.
Yang, W.D., Xiao, J.K., Yu, B.S., Fang, T., Chen, F., Lu, X.J., 1997. The Sedimentology, Geochemistry and Sustainable Development Strategies of Yunnan and Guizhou Phosphorite. Geological Publishing House, Beijing.
Yarincik, K.M., Murray, R.W., Lyons, T.W., Peterson, L.C., Haug, G.H., 2000. Oxygenation history of bottom waters in the Cariaco Basin, Venezuela, over the past 578,000 years: Results from redox-sensitive metals (Mo, V, Mn, and Fe). Paleoceanography 15 (6), 593–604.
Ye, L.J., 1989. Chinese Phosphorite Rock. Science Press, Beijing.
Ye, L.J., Chen, D.F., Chen, Q.Y., Liu, K.W., 1986. Physical enrichment – a new theory on the genesis of industrial phosphorite deposits. Acta Sedimentol. Sin. 4 (3), 23–29 (in Chinese with English abstract).
Yin, C.J., Zhang, Y., Jiang, N.H., 1999. Organic Matters from the Fossil-bearing Phosphorites of the Neoproterozoic Doushantuo Formation in Guizhou, South China. Universitatis Pekinensis (Acta Scientiarum Naturalim) 35 (4), 509–517.
Yin, K.H., Jin, H.Y., Ye, D.S., Zhu, C.L., 2007a. Geologic feature and sedimentary environment of upper Sinian Mofang phosphorite deposit in Fuquan. Geol. Chem. Min. 29 (4), 215–221 (in Chinese with English abstract).
Yin, L., Zhu, M., Knoll, A.H., Yuan, X., Zhang, J., Hu, J., 2007b. Doushantuo embryos preserved inside diapause egg cysts. Nature 446 (7136), 661–663.
Zhang, G.W., Li, S.Z., Dong, Y.P., Liu, S.F., He, D.F., Cheng, S.Y., Lu, R.K., Yao, A.P., 2013. Structure and the problems of the South China continent. Chin. Sci. Bull. 3, 1553–1582 (in Chinese with English abstract).
Zhang, J., Zhang, Q., Chen, D.L., 2004. REE geochemistry of the Xinhua REE - bearing phosphorite deposit, Zhijin County, Guizhou province. Geol. Prospect. 40 (1), 40–44.
Zhang, Y.G., Du, Y.S., Chen, G.Y., Liu, J.Z., Wang, Z.P., Xu, Y.Y., Tan, D.W., Li, L., Wang, D.F., Wu, W.M., 2016. Sedimentary characteristics and mineralization model of high-grade phosphorite in the Sinian Doushantuo Age of Kaiyang area, central Guizhou Province. J. Palaeogeogr. 18 (4), 581–594.
Zhao, D.X., 1985. Pelletal phosphorites of the of Doushantuo Formation in Sinian period. Acta Petrologica Sinica 1, 41–51 (in Chinese with English abstract).
Zhao, D.X., 1989. Microstructures of pisolitic and oolitic phosphorites and their genetic characteristics. Acta Petrologica Sinica 4, 66–75 (in Chinese with English abstract).
Zhou, C.M., 1998. Stratigraphy and sedimentary environment of the Upper Sinian Doushantuo Formation in Weng'an phosphorite deposit, Guizhou Province. J. Stratigraphy 22, 308–314.
Zhou, C.M., Xie, G.W., Mcfadden, K., Xiao, S.H., Yuan, X.L., 2007. The diversification and extinction of Doushantuo-Pertatataka acritarchs in South China: causes and biostratigraphic significance. Geol. J. 42 (3–4), 229–262.
Zhou, J.C., Wang, X.L., 2009. Some neoproterozoic geological events involved in the development of the Jiangnan Orogen. Geol. J. China Univ. 15 (4), 453–459 (in Chinese with English abstract).
Zhou, Y.Z., 1990. On sedimentary geochemistry of siliceous rocks originated from thermal water in Nandan-Hechi basins. Acta Sedimentol. Sin. 8, 75–83 (in Chinese with English abstract).
Zhu, X.K., Peng, Q.Y., Zhang, R.B., An, Z.Z., Zhang, F.F., Yan, B., Li, J., Gao, Z.F., Qin, Y., Pan, W., 2013. Geological and geochemical characteristics of the Daotuo super-large manganese ore deposit at Songtao County in Guizhou Province. Acta Geologica Sinica 87 (9), 1335–1348 (in Chinese with English abstract).